UNIVERSITY OF OKLAHOMA

GRADUATE COLLEGE

SPIN-ORBIT COUPLING EFFECTS IN InSb QUANTUM WELL STRUCTURES

A DISSERTATION

SUBMITTED TO THE GRADUATE FACULTY

in partial fulfillment of the requirements for the

Degree of

DOCTOR OF PHILOSOPHY

By

ARUNA RUWAN DEDIGAMA

Norman, Oklahoma

2009

SPIN-ORBIT COUPLING EFFECTS IN InSb QUANTUM WELL STRUCTURES

A DISSERTATION APPROVED FOR THE
HOMER L. DODGE DEPARTMENT OF PHYSICS AND ASTRONOMY

BY

____
Dr. Sheena Murphy (Chair)

____
Dr. Matthew B. Johnson

____
Dr. Michael B. Santos

____
Dr. Kieran Mullen

____
Dr. Zhisheng Shi

© Copyright by ARUNA RUWAN DEDIGAMA, 2009
All Rights Reserved.

To my parents

ACKNOWLEDGEMENTS

I would like to express my sincere gratitude to my thesis advisor Prof. Sheena Q. Murphy for her guidance, support and encouragement during my research work. Her expertise, patience and understanding have been remarkably helpful to me throughout my graduate studies at The University of Oklahoma.

I am very grateful to my graduate committee members Prof. Matthew B. Johnson, Prof. Michael B. Santos, Prof. Kieran Mullen and Prof. Zhisheng Shi for their support and guidance in completing this work. I would like to acknowledge Prof. Matthew B. Johnson for providing invaluable guidance in nanofabrication instrumentation and Prof. Michael B. Santos for providing high quality InSb quantum well structures. Special thanks to Prof. Kieran Mullen for useful discussions and theoretical simulations, also I would like to thank him for his help in my admission process to the University of Oklahoma.

I would like to thank all the faculty and staff members of the department of Physics and Astronomy for their valuable support during my graduate studies. I would like to make a special thanks to Dr. Preston Larson for his support in SEM imaging and analysis. I am also very grateful for Dr. Joel Keay in providing great deal of support and guidance for the experiments include in this thesis.

I would like to acknowledge my fellow graduate students, Mark Curtis, Dilhani Jayathilaka and Samantha Gunawardana for their assistance in various experiments. Special thanks to REU and undergraduate students for their support on cryostat data acquisition system modifications and software updates.

I am deeply grateful to my parents, Sumanadasa and Pemawathie Dedigama for their support and care. Their guidance immensely helped me to cope with difficult situations in life. I would like to thank my two sisters for their love and understanding.

I would like to express my deepest appreciation to my wife Madhavie for her wonderful support and encouragement during my thesis work. This work would not have been possible without her help. Finally I would like to thank our daughter Chethya for bringing happiness and joy in to our lives.

TABLE OF CONTENTS

ACKNOWLEDGEMENTS…………...………………………………………………...iv

TABLE OF CONTENTS……………...……………………………………………vi

LIST OF FIGURES………...………………………………………………………..x

LIST OF TABLES……………………………………………………………….....xiv

ABSTRACT…………………………………………………………………………..xv

INTRODUCTION…………………………………………………………………...xvii

CHAPTERS

1 Fundamentals of spin-orbit coupling in two-dimensional electron systems……………1

1.1 Introduction…………………………………………………………………..1

1.2 Dresselhaus spin-orbit interaction……………………………………...….6

1.3 Rashba spin-orbit interaction……………………………………………...7

2 Quantum interference effect………………………………………………………….9

2.1 Introduction…………………………………………………………………9

2.2 Characteristic length scales………………………………………………..9

2.2.1 Elastic mean free path…………………………………………..9

2.2.2 Phase breaking length…………………………………………10

2.2.3 Magnetic length………………………………………………….10

2.3 Weak localization………………………………………………………...11

2.4 Weak antilocalization……………………………………………………12

2.5 Transport regimes in weak antilocalization ………………………..…...14

2.6 Theoretical modeling and fitting parameters……………………………15

3 Material system……………………………………………………………...18

3.1 Introduction………………………………………………………………18

3.2 InSb quantum well structures……………………………………….....18

3.3 Physical properties of InSb…………………………………………....21

4 Device fabrication and measurement techniques………………………………23

4.1 Introduction………………………………………………………………23

4.2 Photolithography…………………………………………………………23

4.3 E-beam lithography………………………………………………………25

4.4 Wet etching………………………………………………………………27

4.5 Reactive Ion etching ……………………………………………………28

4.5.1 High density inductively coupled plasma………………………..29

4.5.2 Etching of InSb with $CH_4/H_2/Ar$ based plasma………………….30

4.5.3 Etching of InSb with BCl_3/Ar based plasma…………………….32

4.6 Ohmic contact deposition and annealing…………………………...…35

4.7 Sample mounting and wire bonding……………………………………..35

4.8 Sample thin down……………………………………………………...…37

4.9 Low temperature magnetotransport……………………………………...38

5 Weak antilocalization in InSb quantum wells……………………………..............39
5.1 Introduction………………………………………………………...39
5.2 Temperature dependence of weak antilocalization………………………39
5.3 Gate voltage dependence of WAL for asymmetric samples……………..45
5.4 Weak antilocalization of symmetric samples……………………………49
5.5 Conclusion……………………………………………………………….54

6 Spin polarized magnetotransport in InSb quantum well structures...............................55
6.1 Introduction………………………………………………………...55
6.2 Transverse magnetic focusing of electrons……….…………………...55
6.3 Spin splitting due to spin-orbit interactions…………………………...57
6.4 Transformation of cyclotron orbits from momentum space to real space……………………………………………………………...62
6.5 Spin polarized current focusing of InSb heterostructures………………..63
6.6 Gate voltage dependence of current focusing peaks……………………..68
6.7. Spin filtering of current focusing devices………………………………..69
6.8 Current focusing of asymmetrically doped samples……………………..71
6.9 Conclusions……………………………………………………………77
7 Conclusions and future work……………………………………………..............78
7.1 Introduction……………………………………………………………78
7.2 Conclusion……………………………………………………………78
7.3 Further work…………………………………………………………..79
BIBLIOGRAPHY……………………………………………………….........80

APPENDIX A…………………………………………………………………………....86

APPENDIX B…………………………………………………………………………....87

APPENDIX C…………………………………………………………………………....88

APPENDIX D…………………………………………………………………………....89

LIST OF FIGURES

Figure 1.1 Schematic of potential profile for a heterostructure…………………….....5

Figure 1.2 Band diagram of a direct band gap zincblende structure…………………8

Figure 2.1 Electron transport path with impurity scattering in the absence of spin-orbit interaction………………………………………………………..11

Figure 2.2 (a) Electron transport path with impurity scattering with spin orbit interaction. (b) Characteristic length scales under the influence of the spin-orbit interaction………………………………………………………..13

Figure 3.1 Schematic of s-series sample structure (not to scale) (a) symmetrically doped and (b) asymmetrically doped……………………………………19

Figure 3.2 Schematic of t-series sample structure (not to scale) (a) symmetrically doped and (b) asymmetrically doped…………………………………....21

Figure 4.1 Schematic (not to scale) of typical positive photolithography steps…....24

Figure 4.2 Block diagram showing the major components of a typical electron beam lithography system…………………………………………………….26

Figure 4.3 Schematic diagram of (a) sputtering, (b) chemical, (c) ion-enhanced, and (d) sidewall inhibitor etch mechanisms……………………………….28

Figure 4.4 Schematic diagram of inductively coupled plasma (ICP) etch system……………………………………………………………….....30

Figure 4.5 SEM micrographs of InSb samples etched with CH_4/H_2/Ar RIE with CH_4/H_2 ratio of (a) 15.8%, (b) 30%, (c) 70%...31

Figure 4.6 Solid material formation after RIE (RF power = 120W)………………...33

Figure 4.7 RIE etch rate vs. RF power…………….…………………….……….33

Figure 4.8 SEM micrographs of InSb samples etched with BCl_3/Ar RIE with BCl_3 = 2sccms, Ar = 8 sccms and ICP Power = 0W (a) RF Power = 60W, (b) RF Power = 120W (c) RF Power = 180W…………………………..……34

Figure 4.9 SEM micrograph of 200 nm RIE trench with the optimized recipe………………………………………………………………….35

Figure 4.10 Schematic of sample cleaving steps……………………………………..36

Figure 4.11 28-Pin PLCC with three wire bonded Hall bars…………………………37

Figure 5.1 Experimental magnetoconductivity σ(B)-σ(0) of sample T162 for different temperatures…………………………………………………………...40

Figure 5.2 Experimental magnetoconductivity σ(B)-σ(0) of sample T265 for different temperatures…………………………………………………………...41

Figure 5.3 Phase breaking rate as a function of temperature for sample T162 and T265...……………………………………………………………………43

Figure 5.4 Electron densities as a function of back gate voltage for sample T134.....45

Figure 5.5 Weak antilocalization conductivity correction measured at different carrier densities. ………………………………………………………………46

Figure 5.6 Dependence of spin-orbit length for HLN fittings on the electron density of the quantum well……………………………………….............48

Figure 5.7 Behavior of α values extracted from HLN fittings on the carrier density……………………………………………………………………49

Figure 5.8 HLN fitting for S372 at 4.2K………………………...………………..50

Figure 5.9 HLN fitting for S912 at 4.2K……………………...…………………..51

Figure 5.10 Conductivity corrections for S862 and S901 along with HLN fittings……52

Figure 6.1 Schematic of the transverse electron focusing geometry ……..56

Figure 6.2 Energy eigenstates of spin-split bands due to the Dresselhaus spin-orbit interaction……..58

Figure 6.3 Energy dispersion relations for spin-split bands due to the Rashba spin-orbit interaction……59

Figure 6.4 Fermi energy contours and spin quantization directions for spin-orbit. (a) Rashba spin-orbit interaction; (b) Dresselhaus spin-orbit interaction; (c) Equal amplitudes of Rashba and Dresselhaus terms……..60

Figure 6.5 Energy dispersion relations for unperturbed bands (red dotted line) and spin spilt bands (green and blue solid lines)……..61

Figure 6.6 (a) spin-split energy contours due to spin-orbit interaction linear in momentum; (b) Projection of k- space orbits onto real space……..62

Figure 6.7 SEM micrographs for a typical electron focusing device……..64

Figure 6.8 Transverse magnetic focusing data for Insb/$Al_xIn_{1-x}Sb$ heterostructures at 4.2K for device FOC41……....65

Figure 6.9 Nature of 1st and 2nd transverse magnetic focusing peaks for InSb/$Al_xIn_{1-x}Sb$ heterostructures at 4.2K……...66

Figure 6.10 Temperature evolution of transverse magnetic focusing peaks for InSb/$Al_xIn_{1-x}Sb$ heterostructures……67

Figure 6.11 Gate leakage measurements for the constrictions for a typical current focusing device...……………………………………………………..68

Figure 6.12 Robust nature of focusing peaks for different detector gate voltages........69

Figure 6.13 Schematic of the sample tilter setup for fixed magnetic field………..…70

Figure 6.14 Evolution of the 1st focusing peak with different in-plane magnetic fields…………………………………………………………...71

Figure 6.15 Transverse magnetic focusing data for asymmetrically doped Insb/$Al_xIn_{1-x}Sb$ heterostructures at 4.2K. ……………………………………….72

Figure 6.16 Doublet structure of 1st transverse magnetic focusing peak for asymmetrically doped InSb/AlxIn1-xSb heterostructure………………...73

Figure 6.17 Fermi contours of spin-split bands under the influence of Dresselhaus and Rashba spin orbit interaction……………………………….........74

Figure 6.18 SEM micrographs of (a) 90 degree; (b) 135 degree electron focusing device……………………………………………………………75

Figure 6.19 Transverse magnetic focusing data for asymmetrically doped 90 degree focusing device (a) w=0.3 μm; l=0.3 μm : (b) w = 0.4 μm ; l = 0.3 μm at 4.2K………………………………..76

LIST OF TABLES

Table 3.1 Comparison of basic parameters of InSb with other III-V semiconductor materials ………..…………………………………………………………...22

Table 5.1 Sample parameters for InSb/AlInSb heterostructures…………….............39

Table 5.2 Important length and time scales obtained from HLN fittings for different temperatures………………………………………………...………42

Table 5.3 Extracted length scales obtained from HLN fittings for different carrier densities……………………………………………………………..47

Table 5.4 Sample parameters for symmetrically doped InSb/AlInSb heterostructures……………………………………………………......50

Table 5.5 HLN fitting parameters along with extracted Dresselhaus spin-orbit constants for different τ_1/τ_3 ratios…………...…………………………53

ABSTRACT

Indium antimonide (InSb) is a narrow band gap material which has the smallest electron effective mass ($0.014m_0$) and the largest electron Lande g-facture (-51) of all the III-V semiconductors. Spin-orbit effects of III-V semiconductor heterostructures arise from two different inversion asymmetries namely bulk inversion asymmetry (BIA) and structural inversion asymmetry (SIA). BIA is due to the zinc-blende nature of this material which leads to the Dresselhaus spin splitting consisting of both linear and cubic in-plane wave vector terms. As its name implies SIA arises due to the asymmetry of the quantum well structure, this leads to the Rashba spin splitting term which is linear in wave vector.

Although InSb has theoretically predicted large Dresselhaus (760 eV$Å^3$) and Rashba (523 e$Å^2$) coefficients there has been relatively little experimental investigation of spin-orbit coefficients. Spin-orbit coefficients can be extracted from the beating patterns of Shubnikov–de Haas oscillations (SdH), for material like InSb it is hard to use this method due to the existence of large electron Lande g-facture. Therefore it is essential to use a low field magnetotransport technique such as weak antilocalization to extract spin-orbit parameters for InSb.

The main focus of this thesis is to experimentally determine the spin-orbit parameters for both symmetrically and asymmetrically doped InSb/$In_xAl_{1-x}Sb$ heterostructures. During this study attempts have been made to tune the Rashba spin-orbit coupling coefficient by using a back gate to change the carrier density of the samples. Dominant phase breaking mechanisms for InSb/$In_xAl_{1-x}Sb$ heterostructures have been identified by analyzing the temperature dependence of the phase breaking field from weak antilocalization

measurements. Finally the strong spin-orbit effects on $InSb/In_xAl_{1-x}Sb$ heterostructures have been demonstrated with ballistic spin focusing devices.

INTRODUCTION

Operations of conventional electronic devices rely on the charge of the carriers transported through their active region. These conventional electronic devices have ignored the spin of charged carriers although the existence of spin has been known for a long period of time. The spin of the charged carriers in addition to their charge holds potential for device applications for both metal and semiconductor based spintronic devices.

Although metal based spintronic devices such as giant magneto resistor (GMR) devices are commercially available, semiconductor based hybrid devices have more versatility due to their ability to control the motion of charged carriers via spin-orbit interaction, which arises due to lack of inversion symmetry of the crystal structure and growth. Recently there has been considerable amount of interest in spin-orbit interaction in semiconductor heterostructures for various device applications.

It has been theoretically predicted that InSb has strong spin-orbit effects. This interesting property makes InSb a promising material for spintronic applications. Additionally a high mobility at room temperature makes this material a viable candidate for fast switching field-effect transistors and ballistic transport devices.

In this thesis we report experimental measurements of Dresselhaus and Rashba coefficients via weak anti-localization on InSb quantum wells. The samples are $InSb/Al_xIn_{1-x}Sb$ heterostructures grown on GaAs substrates using molecular beam epitaxy (MBE). In order to measure the effects of Dresselhaus and Rashba spin-orbit interactions separately we use two series of samples (symmetrically and asymmetrically doped) in

which each series has samples with different electron densities. Our experiment involves measuring low field magneto-conductance in which strong spin-orbit coupling leads to destructive interference. The last part of this thesis reports spin filtering current focusing devices due to strong spin-orbit coupling in InSb. The organization of this thesis as follows.

Chapter 1: Fundamentals of spin-orbit coupling in two-dimensional electron systems

The origin of spin-orbit interaction is introduced starting from the Dirac equation for spin $1/2$ particles. The concept was extended to semiconductor heterostructures paying attention to the local electric fields arising from lack of inversion symmetries namely bulk inversion asymmetry and structural inversion asymmetry.

Chapter 2: Quantum interference effect

The main focus of this thesis is to investigate the strength of spin-orbit interactions in $InSb/Al_xIn_{1-x}Sb$ heterostructures using weak antilocalization. In this chapter we discuss the fundamental concepts of weak antilocalization, the characteristic lengths and the theoretical modeling.

Chapter 3: Material system

Weak antilocalization strongly depends on the mobility and carrier density of the structure considered. Also in order to understand the relative strength of Rashba spin-orbit interaction, it is important to know the parameters such as quantum well width, spacer layer thickness and information about δ-doping etc. In this chapter a brief description of quantum well structures used in our experiments will be discussed.

Chapter 4: Device fabrication

To produce nanometer scale semiconductor devices, proper use of sophisticated processing techniques are required. Since InSb is not so common compared to materials like Si or GaAs, standard processing recipes for InSb are rare in literature. Virtually for every processing step, we had to develop recipes suited for InSb/$Al_xIn_{1-x}Sb$ systems. This chapter introduces various processing techniques and recipes used to fabricate our devices.

Chapter 5: Weak antilocalization in InSb quantum wells

In this chapter we discuss the results of our experimental investigations on weak antilocalization. This chapter also includes the interpretation of experimental data using appropriate theoretical models and details on extracted spin-orbit parameters for InSb/$Al_xIn_{1-x}Sb$ heterostructures.

Chapter 6: Spin polarized magnetotransport on InSb quantum well structures

Experimental efforts to demonstrate spin polarization and spin filtering through cyclotron motion of electrons under the influence of spin-orbit interaction are discussed in this chapter. Also an attempt has been made to estimate the strength of spin-orbit interaction from the spin resolved focusing peaks.

Chapter 7: Conclusions and future work

This chapter includes a summary of the experiments we performed for this thesis and future work which has to be done in order to improve upon these experiments.

Chapter 1

Fundamentals of spin-orbit coupling in two-dimensional electron systems

1.1 Introduction

The spin-orbit interaction is responsible for lifting the degeneracy of electron energy levels in many atoms, molecules and solids. The origin of spin-orbit coupling is due to the relativistic nature of electron motion. This can be derived from the Dirac equation of spin $1/2$ particles and appears in the Schrödinger equation as a first order relativistic correction. To get an expression for the spin-orbit interaction one starts with the Dirac equation using the relativistic expression for the kinetic energy of electrons [1].

$$H^2 = c^2 \boldsymbol{p}^2 + m^2 c^4 \qquad 1.1$$

For the non-relativistic Hamiltonian, electric and magnetic potentials ϕ and $\boldsymbol{A}$ can be introduced by the substitutions $\boldsymbol{p} \rightarrow \boldsymbol{p} - \left({(q)}/{c} \right)\boldsymbol{A}$ and $H \rightarrow H - q\phi$ where q is the electron charge $-e$. With the relativistic kinetic energy correction the Hamiltonian in equation 1.1 is modified as follows;

$$\left(H - q\phi \right)^2 = \left(c\boldsymbol{p} - q\boldsymbol{A} \right)^2 + m^2 c^4 \qquad 1.2$$

One can obtain the relativistic wave equation for an electron in an external electric and magnetic field by representing H and $\boldsymbol{p}$ in terms of their quantum mechanical

operators $H = i\hbar\frac{\partial}{\partial t}$; $\boldsymbol{p} = -i\hbar\nabla$ in equation 1.2 and then acting on the electron wave function ψ .

In the case of a free electron, the relativistic wave equation can be obtained by applying the same procedure to equation 1.1 and has the following format

$$\left(H^2 - c^2\sum_{\mu} p_{\mu}^2 - m^2c^4\right)\psi = 0$$
$$\text{or} \qquad 1.3$$
$$-\hbar^2\frac{\partial^2}{\partial t^2}\psi = -\hbar^2c^2\nabla^2\psi + m^2c^4\psi$$

Here $\left(p_{\mu} = p_x, p_y, p_z\right)$ are the components of the momentum operator. This is a second order differential equation in t and therefore initial values of ψ and $\frac{\partial\psi}{\partial t}$ are required to solve it whereas the Schrödinger equation only needs the initial value of ψ .

Dirac approached this problem by splitting this expression into a product of two linear equations and considered them individually. The Dirac formalism for the force free form of equation 1.3 has the following format

$$\left(H - c\sum_{\mu}\alpha_{\mu}p_{\mu} - \beta mc^2\right)\left(H + c\sum_{\mu}\alpha_{\mu}p_{\mu} + \beta mc^2\right)\psi = 0 \qquad 1.4$$

The constant coefficients α_{μ} and β satisfy the relations in equation 1.5

$$\begin{aligned} &\alpha_{\mu}\alpha_{\mu'} + \alpha_{\mu'}\alpha_{\mu} = 2\delta_{\mu\mu'} \\ &\alpha_{\mu}\beta + \beta\alpha_{\mu} = 0 \\ &\beta^2 = 1 \end{aligned} \qquad 1.5$$

One can easily verify this by multiplying the product in equation 1.4 and substituting the relations in 1.5. Equation 1.4 can be solved by solving the first part of the product which is shown in equation 1.6,

$$\left(H - c\sum_{\mu}\alpha_{\mu}p_{\mu} - \beta mc^2\right)\psi = 0 \qquad 1.6$$

This is a first order differential equation in t and is referred to as the linearized version of the Dirac equation.

To compare the Dirac equation with the Schrödinger equation in an external electromagnetic field, we must again use the substitutions $\boldsymbol{p} \to \boldsymbol{p} - \left(q/c\right)\boldsymbol{A}$ and $H \to H - q\phi$ for $\boldsymbol{p}$ and H and use the non-linearized version of equation 1.4. It then has the following form.

$$\left[\left(H - q\phi - \boldsymbol{\alpha}.\left(c\boldsymbol{p} - q\boldsymbol{A}\right) - \beta mc^2\right)\times\left(H - q\phi + \boldsymbol{\alpha}.\left(c\boldsymbol{p} - q\boldsymbol{A}\right) + \beta mc^2\right)\right]\psi = 0$$

1.7 We can simplify equation 1.6 by defining electric and magnetic field strengths in terms of the potentials $\boldsymbol{E} = -\frac{1}{c}\frac{\partial \boldsymbol{A}}{\partial t} - \nabla\phi$ and $\boldsymbol{B} = \nabla \times \boldsymbol{A}$.

Using $H = W + mc^2$ and assuming that the kinetic and potential energies are small compared to rest mass energy mc^2, two components of the spin function can be neglected. Under this condition equation 1.7 simplifies to the following form.

$$\left\{\frac{1}{2m}\left(\boldsymbol{p} - \frac{q}{c}\boldsymbol{A}\right)^2 + q\phi - \frac{q\hbar}{2mc}\boldsymbol{\sigma}.\boldsymbol{B} + i\frac{q\hbar}{4m^2c^2}\boldsymbol{E}.\boldsymbol{p} - \frac{q\hbar}{4m^2c^2}\boldsymbol{\sigma}.\left[\boldsymbol{E}\times\boldsymbol{p}\right]\right\}\psi = W\psi \qquad 1.8$$

where $\boldsymbol{\sigma}$ are the Pauli spin matrices. In the above expression the first two terms are exactly as those of the non-relativistic Schrödinger equation for an external electromagnetic field. The third term represents the interaction energy $-\boldsymbol{\mu}.\boldsymbol{B}$ between a magnetic dipole $\boldsymbol{\mu}$ and the external magnetic field $\boldsymbol{B}$. The magnetic dipole moment can

be represented by the operator $\boldsymbol{\mu} = \left({q\hbar}/{2mc} \right)\boldsymbol{\sigma}$. The fourth term does not have a classical analog and it is the relativistic correction to the energy.

Using the principles of classical electrodynamics, it can be shown that the vectors of the electromagnetic field are dependent on the frame of reference [3]. An observer in a reference frame moving with velocity $\boldsymbol{v}$ relative to an electric field $\boldsymbol{E}$ finds a magnetic field $\boldsymbol{B}$. This Lorentz transformed magnetic field has the form

$$\boldsymbol{B} = -\frac{c^{-1}\boldsymbol{v} \times \boldsymbol{E}}{\sqrt{1-\left({v}/{c} \right)^2}} \qquad 1.9$$

By neglecting the higher order terms of ${v}/{c}$ one can approximate the effective magnetic field as

$$\boldsymbol{B} = -\frac{1}{c}\left(\boldsymbol{v} \times \boldsymbol{E} \right) = \frac{1}{mc}\left(\boldsymbol{E} \times \boldsymbol{p} \right) \qquad 1.10$$

The energy of an electron moving relative to a static electric field can be written as.

$$-\boldsymbol{\mu}.\boldsymbol{B} = -\left[\left({q\hbar}/{2mc} \right)\boldsymbol{\sigma} \right].\left[\frac{1}{mc}\left(\boldsymbol{E} \times \boldsymbol{p} \right) \right] = -\frac{q\hbar}{2m^2c^2}\boldsymbol{\sigma}.\left(\boldsymbol{E} \times \boldsymbol{p} \right) \qquad 1.11$$

Therefore it is quite evident that the last term in equation 1.8 is a direct consequence of the coupling of the electron spin with the effective magnetic field generated from the Lorentz transformed electric field and hence is known as the spin-orbit energy.

However the energy term in equation 1.11 is a factor of two greater than the last term in expression 1.8. The change of the precession frequency of the electron spin in the magnetic field has not been taken into consideration when changing the frame of reference and hence the factor of two.

If the motion of the electron takes place in a spherically symmetric potential $\phi(r)$ such as for the orbital motion of an electron under the influence of the electric field of an atomic nucleus, the resulting electric field $\boldsymbol{E}$ is given by;

$$\boldsymbol{E} = -q^{-1}\left(\frac{d\phi(r)}{dr}\right)\hat{\boldsymbol{r}} \qquad 1.12$$

Then the spin-orbit term for the central potential can be obtained in the following form

$$-\frac{q\hbar}{4m^2c^2}\boldsymbol{\sigma}.(\boldsymbol{E}\times\boldsymbol{p}) = \left(\frac{-q\hbar}{4m^2c^2}\right)\boldsymbol{\sigma}.\left(-q^{-1}\left(\frac{d\phi(r)}{dr}\right)\hat{\boldsymbol{r}}\times\boldsymbol{p}\right) = \frac{\hbar}{4m^2c^2}\left(\frac{d\phi(r)}{dr}\right)\boldsymbol{\sigma}.(\hat{\boldsymbol{r}}\times\boldsymbol{p}) \qquad 1.13$$

This expression represents the interaction of the magnetic moment of the electron with the effective magnetic field. From equation 1.13, it can be seen that the contribution to the Hamiltonian due to the spin orbit interaction has the form,

$$H_{so} \sim \left(\frac{d\phi(r)}{dr}\right)\hat{\boldsymbol{r}}.(\boldsymbol{\sigma}\times\boldsymbol{p}) \qquad 1.14$$

However in the case of semiconductor heterostructures electric fields can be generated in two ways, one due to the lack of inversion symmetry of the crystal structure and the other due to the asymmetry of confinement potential of the growth structure as shown in figure 1.1.

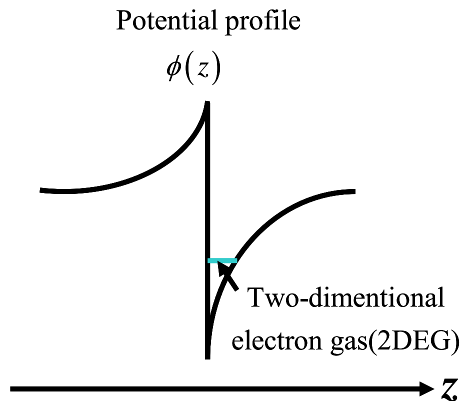

Figure 1.1 Schematic of potential profile for a heterostructure

1.2 Dresselhaus spin-orbit interaction

The majority of III-V compound semiconductor materials have a zincblende crystal lattice structure. The zincblende structure consists of two interpenetrating face centered cubic (FCC) sub lattices, one containing group III atoms and the other containing group V atoms. The two sub-lattices are shifted relative to each other by $(a/4, a/4, a/4)$ where a is the cubic lattice constant.

Dresselhaus S-O coupling is due to the lack of inversion symmetry between the two different types of atoms [4]. Treating this S-O coupling as a perturbation the Hamiltonian for spin splitting in the conduction band for a bulk material has the following form [5].

$$H_{so} = \gamma \sum_i \sigma_i k_i \left(k_{i+1}^2 - k_{i+2}^2 \right) \qquad i = x, y, z \;\; and \;\; i + 3 = i \tag{1.15}$$

where γ is the Dresselhaus S-O coupling constant. For a semiconductor quantum well (QW) grown in the $[001]$ direction, the confinement gives rise to quantization of k_z resulting in $\langle k_z \rangle = 0$ and hence the Hamiltonian in equation 1.15 becomes

$$H = \frac{k^2}{2m^*} + (\boldsymbol{\sigma}_x . \boldsymbol{\Omega}_x) + (\boldsymbol{\sigma}_y . \boldsymbol{\Omega}_y) \tag{1.16}$$

where $k = (k_x, k_y)$ is the in-plane wave vector and $\boldsymbol{\Omega} = (\boldsymbol{\Omega}_x, \boldsymbol{\Omega}_y)$ is the spin orbit frequency vector in the plane of the quantum well which can be expanded from orthogonal spherical harmonics as shown in equation 1.17. The magnitude of the vector

$2\Omega/\hbar$ represents the frequency of spin precession and its direction defines the axis of precession. The resulting spin splitting is given by 2Ω.

$$\begin{aligned}
\Omega_x &= \gamma\left[k_x\left(k_y^2-\left\langle k_z^2\right\rangle\right)\right]=-\Omega_{D1}\cos(\phi)-\Omega_{D3}\cos(3\phi) \\
\Omega_y &= \gamma\left[k_y\left(\left\langle k_z^2\right\rangle-k_x^2\right)\right]=-\Omega_{D1}\sin(\phi)-\Omega_{D3}\sin(3\phi) \\
\tan(\phi) &= \frac{k_x}{k_y} \quad ; \quad k^2=k_x^2+k_y^2 \\
\Omega_{D1} &= \gamma k\left[\left\langle k_z^2\right\rangle-\frac{1}{4}k^2\right] \quad ; \quad \Omega_{D3}=\gamma\frac{k^3}{4} \\
\Omega^2 &= \Omega_x^2+\Omega_y^2
\end{aligned} \qquad 1.17$$

The terms Ω_{D1} and Ω_{D3} are the so called linear and cubic Dresselhaus terms and $\left\langle k_Z^2\right\rangle$ is the average squared of the wavevector in z direction.

1.3 Rashba spin-orbit interaction

The Rashba spin-orbit interaction is generated by the asymmetry of the layer structure. This can include asymmetric doping, gating on one side and an asymmetry at the interfaces of the quantum well. In the case of asymmetric doping, the electric field generated is perpendicular to the 2DEG [5]. The Rashba S-O Hamiltonian has the form

$$H_R = \alpha[\boldsymbol{\sigma}\times\boldsymbol{k}]_z \qquad 1.18$$

This term can be included in the Hamiltonian in expression 1.16 by adding the following terms to spin precession frequency $2\Omega/\hbar$.

$$\begin{aligned}
&\Omega_x = \Omega_R\sin(\phi), \quad \Omega_y = -\Omega_R\cos(\phi) \\
&\Omega_{R1} = \alpha k
\end{aligned} \qquad 1.19$$

The spin-splitting parameter α is known as the Rashba coefficient and has two different contributions from the layer structure. The main contribution is from the electric field in

the quantum well. There is a second contribution from leakage of the electron wave function into the barriers due to finite barrier heights of the layer structure [6].

However if we consider the only the electric field then α can be written in terms of electric field as shown in equation 1.19 [7].

$$\alpha = \alpha_0 \left\langle \left| \vec{E}_Z \right| \right\rangle$$

$$\alpha_0 = \frac{\hbar^2}{2m^*} \frac{\Delta}{E_g} \frac{2E_g + \Delta}{\left(E_g + \Delta\right)\left(3E_g + 2\Delta\right)} e \qquad 1.20$$

where E_g the band is gap energy and Δ is the split-off energy. Unlike the Dresselhaus terms, the Rashba contribution only has a *k*-linear dependence. The Rashba spin-orbit coupling constant α can be changed by applying an external electric field, a desirable effect for device applications.

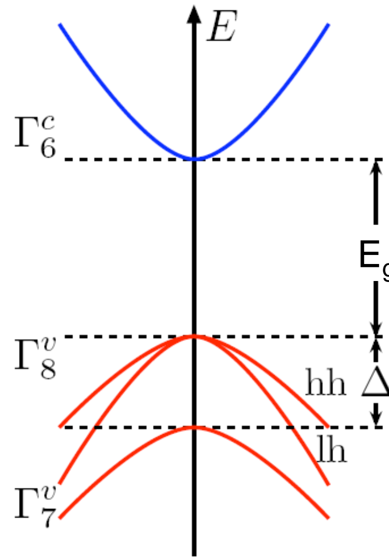

Figure 1.2 Band diagram of a direct band gap zincblende structure

Chapter2

Quantum interference effect.

2.1 Introduction

The quantum mechanical description of an electron wave function $\psi(r)$ requires both an amplitude $A(r)$ and a phase factor ϕ which can be written as $\psi(r) = A(r)e^{i\phi}$, while the phase factor has no effect on classical transport, it plays an important role in quantum interference which is the underlying principle of the Aharonov-Bohm (AB) effect, weak localization (WL) and weak antilocalization (WAL) [8,9]. I will start with a description of some characteristic length scales and then return to the role of phase in quantum transport.

2.2 Characteristic length scales

2.2.1 Elastic mean free path (l_e)

In a real electronic system electrons are scattered by defects in the crystal, impurities and phonons. The elastic mean free path is the average distance electrons travel before undergoing elastic scattering events. It can be expressed in terms of a Fermi velocity v_F and τ_{tr} the transport relaxation time

$$l_e = v_F \tau_{tr} \qquad 2.1$$

where τ_{tr} is determined by $\frac{1}{\tau_{tr}} = \int (1 - \cos\theta) W(\theta) d\theta$ 2.2

Here $W(\theta)$ is the probability that the electron wave vector changes direction by an angle θ per unit time due to elastic scattering [5]. It is customary to refer l_e as the transport length l_{tr}.

2.2.2 Phase breaking length (l_ϕ)

As mentioned in the introduction, the wave function also requires a phase factor. An electron moves without losing its phase over a characteristic length, l_ϕ [10]. Beyond this length electrons lose their initial phase by inelastic scattering. Inelastic scattering events such as those due to scattering by phonons, electron-electron collisions and spin-flip scattering and which break the time reversal symmetry are responsible for phase relaxation. In between single phase breaking scattering processes, electrons can suffer many elastic scattering events hence the expression for l_ϕ uses the diffusion constant D along with phase breaking time τ_φ, instead of v_F.

$$l_\varphi = \left(D\tau_\varphi\right)^{\frac{1}{2}} \text{ where } D = \frac{v_F^2 \tau_{tr}}{2} \qquad 2.3$$

At low temperature where electron-electron scattering is dominant, l_ϕ depends on the temperature of the system.

2.2.3 Magnetic length (l_B)

In the presence of an external magnetic field, there is another length scale to consider, the magnetic length. This characteristic length is the spatial extent of the wavefunction in a field and is given by [10]

$$l_B = \left(\frac{\hbar}{eB}\right)^{\frac{1}{2}} \qquad 2.4$$

2.3 Weak localization

Weak localization (WL) is a quantum correction to the classical conductivity due the coherent nature of scattering events. This was first predicted by Anderson in 1958 [11, 12]. For a system without any spin-orbit interaction, the presence of disorder results in a non-zero probability for the electron to return to the initial position after a number of scattering events. For every clockwise trajectory shown below, there will be a counterclockwise trajectory in which the electron travels in the same path, but in the opposite direction (see Figure 2.1) [13].

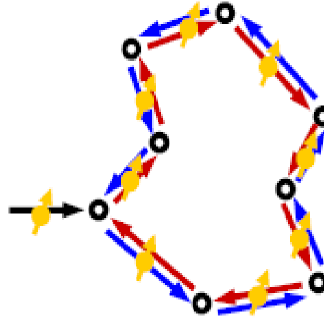

Figure 2.1 Electron transport paths with impurity scattering in the absence of spin-orbit interaction

According to time reversal symmetry, two electron waves traveling on such identical but reversed trajectories acquire the same phase factor resulting constructive interference when they combine at the origin. This can be explained more rigorously if one considers the probability amplitudes A_f and A_b of two time reversed trajectories, then the coherent back scattering probability has the form [14]:

$$\left|\sum_i A_i\right|^2 = \sum_i |A_i|^2 + \sum_{i\neq j} A_i A_j^*$$
$$|A_f + A_b|^2 = \left[A_f^2 + A_b^2\right] + \left[A_f A_b^* + A_b A_f^*\right] \quad 2.5$$

Time-reversal invariance guarantees that the forward and backward probability amplitudes around a closed path are identical, 2.5 then reduces to $\left|A_f + A_b\right|^2 = 4\left|A_f\right|^2$ which is twice the classical result. This increase of back scattering probability is known as weak localization, because the conductivity is reduced over the classical result. This constructive interference can be destroyed by breaking the time reversal symmetry by means of an applied external magnetic field.

2.4 Weak antilocalization

The presence of the spin-orbit interaction does not affect time reversal symmetry, however now the spin rotation acquired by an electron traveling on a closed path trajectory is opposite to that acquired on the time reversed trajectory. Assuming the initial spin state is $\left|s\right\rangle$, the final spin states $\left|s^{'}\right\rangle$ and $\left|s^{"}\right\rangle$ of electrons on the time reversal paths can be expressed in terms of the spin rotation operator R [15].

$$\begin{aligned} \left|s^{'}\right\rangle &= R\left|s\right\rangle \\ \left|s^{"}\right\rangle &= R^{-1}\left|s\right\rangle \end{aligned} \qquad 2.6$$

R has the property $RR \;\; = 1$, hence the interference term becomes $\left\langle s^{'}\left|R^2\right|s^{"}\right\rangle = -1/2$. The negative sign is due to the opposite spin rotation along the two paths. Compared to WL this quantum contribution has the opposite sign and is half as much. This correction decreases the coherent back scattering probability resulting an increase in conductivity at $B = 0$. The phenomenon is known as weak antilocalization (WAL) and like WL can also be destroyed by applying an external magnetic field which introduces an additional phase accumulation around the closed loop. When discussing systems with spin-orbit

interaction, it is appropriate to introduce yet another length scale, l_{so} the spin orbit length, which is defined as the length over which the spin acquires a shift of the order of π due to the coupling between the spin and the orbital motion.

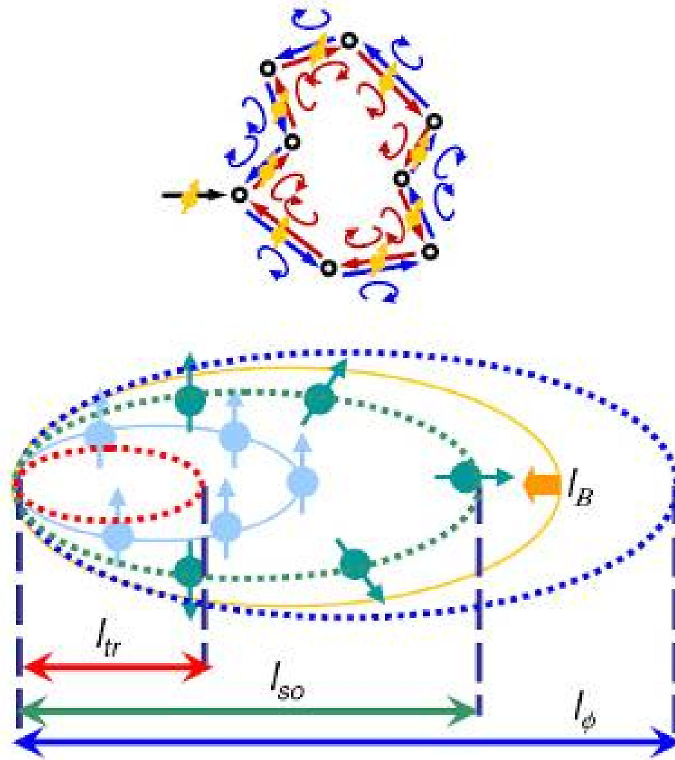

Figure 2.2 (a) Electron transport paths with impurity scattering with spin-orbit interaction. (b) Characteristic length scales under the influence of the spin-orbit interaction

Figure 2.2 provides a schematic description of WAL in the diffusive limit where all relevant length scales are greater than l_{tr}. If there is a closed path for the electron trajectory of the scale of l_{bs} which satisfies the condition $l_\phi > l_{bs} > l_{so}$ [13], then the path contributes to WAL. For $l_{bs}>l_\phi$ electrons lose their phase information and the paths do not contribute any quantum correction. In the limit $l_{so} > l_{bs} > l_{tr}$, the path length traversed is not sufficient to result in much phase rotation and the overall quantum correction yields

constructive interference (WL). For a 2DEG of low mobility and high spin-orbit interaction the characteristic length scales preserve the order $l_{\phi} > l_{so} > l_{tr}$ as shown in Figure 2.2 (b), therefore WAL can be observed in the magnetoconductance measurements. The introduction of a weak magnetic field introduces yet another length scale, l_B. For trajectories of this scale, the phase shift generated by the vector potential compensates that acquired by the spin-orbit interaction. For larger magnetic fields, l_B becomes even shorter and once l_B is shorter than l_{SO}, the phase shift is no longer sufficient to generate a destructive contribution and the magnetoconductance becomes positive. For $l_{tr} >> l_B$ electron cyclotron motion comes into play and the magnetoconductance starts to oscillate.

2.5 Transport regimes in weak antilocalization

Since WAL depends on the strength of spin-orbit interaction, we can use the magnetoconductance data to extract spin-orbit parameters. WAL data can be acquired in two different regimes, namely "diffusive" and "ballistic". These regimes are defined by the relative magnitudes of the magnetic length l_B and the electron mean free path l_{tr} [16]. For the diffusive regime $l_B > l_{tr}$ whereas the opposite limit is the case for the ballistic limit.

2.6 Theoretical modeling and fitting parameters

For symmetrically doped III-V quantum wells grown in the $[001]$ direction, Iordanskii, Lyanda-Geller, Pikus (ILP) [17] developed a theoretical model for weak antilocalization

conductivity correction for the case of a weak spin-orbit interaction. The weak localization correction is expressed in terms of Cooperon amplitude by taking only the Dresselhaus spin-orbit coupling into consideration and solving the Cooperon amplitude using perturbation theory. In depth analysis of the derivation of the ILP model is beyond the scope of this thesis. I only report the final solution here. This model consists of three different fitting parameters namely H_ϕ, H_{so} and H'_{so}. The expression to the conductivity correction has the following form.

$$\Delta\sigma(B) = -\frac{e^2}{4\pi^2\hbar}\left\{ \begin{array}{c} \dfrac{1}{a_0} + \dfrac{2a_0 + 1 + \left(H_{so}/B\right)}{a_1\left[a_0 + \left(H_{so}/B\right)\right] - \left(2H'_{so}/B\right)} \\ -\displaystyle\sum_{n=1}^{\infty}\left[\dfrac{3}{n} - \dfrac{3a_n^2 + 2a_n\left(H_{so}/B\right) - 1 - 2(2n+1)\left(H'_{so}/B\right)}{\left[a_n + \left(H_{so}/B\right)\right]a_{n-1}a_{n+1} - 2\left(H'_{so}/B\right)\left[(2n+1)a_n - 1\right]}\right] \\ + 2\ln\dfrac{H_{tr}}{B} + \psi\left(\dfrac{1}{2} + \dfrac{H_\phi}{B}\right) + 3C \end{array} \right\} \qquad 2.7$$

where

$$a_n = n + \frac{1}{2} + \frac{H_\phi}{B} + \frac{H_{SO}}{B}, H_\phi = \frac{c\hbar}{4eD\tau_\varphi}, H_{so} = \frac{c\hbar}{4eD}\left(2\Omega_{1D}^2\tau_1 + 2\Omega_{3D}^2\tau_3\right)$$
$$H'_{so} = \frac{c\hbar}{4eD}2\Omega_{1D}^2\tau_1, H_{tr} = \frac{c\hbar}{4eD\tau_1}, \psi(1+z) = -C + \sum_{n=1}^{\infty} - \frac{z}{n(n+z)} \qquad 2.8$$

In here C is the Euler constant and $\tau_n, n = 1,2,3$ is the phase relaxation time of the respective components of the distribution function $\tau_n^{-1} = \int W(\theta)(1-\cos n\theta)d\theta$ where

$W(\theta)$ is the probability distribution function of scattering by an angle θ. The two parameter WL conductivity correction pioneered by Hikami, Larkin-Nagoaka (HLN) [18] can be obtained from ILP model by neglecting H'_{so}/B in expression 2.7, and has the following form

$$\Delta\sigma(B)-\Delta\sigma(0)=\frac{e^2}{2\pi^2\hbar}\left\{\begin{array}{l}\psi\left(\frac{1}{2}+\frac{H_\phi}{B}+\frac{H_{so}}{B}\right)+\frac{1}{2}\psi\left(\frac{1}{2}+\frac{H_\phi}{B}+\frac{2H_{so}}{B}\right)-\psi\left(\frac{1}{2}+\frac{H_\phi}{B}\right)\\ -\ln\left(\frac{H_\phi}{B}+\frac{H_{so}}{B}\right)-\frac{1}{2}\ln\left(\frac{H_\phi}{B}+\frac{2H_{so}}{B}\right)+\frac{1}{2}\ln\frac{H_\phi}{B}\end{array}\right\} \quad 2.9$$

Both the ILP and HLN models are only valid for the diffusive regime and only one type of spin-orbit interaction can be taken into account. Depending on the relative strength between Dresselhaus and Rashba spin-orbit interaction one chooses the dominant effect to fit. When both spin-orbit interaction terms are comparable, a numerical diagonalization is required for the Hamiltonian in order to get the WAL conductivity correction [19].

In the ballistic regime the electron spin will rotate considerably between elastic scattering events [20]. Theoretical models have been developed [16,21] to treat the ballistic case by introducing an operator $\boldsymbol{p}$ for the probability of an electron to move forward and backward in a closed path using advanced and retarded Green's functions. The Cooperon has been calculated from $\boldsymbol{p}$ in order to get the weak localization correction as shown in 2.10.

$$\nabla\sigma(B)=-\frac{e^2}{4\pi^2\hbar}\left[\sum_{m=-1,0,1}C\left(x_{1m},f_{1m}\right)-C\left(x_{00},f_{00}\right)\right] \quad 2.10$$

Where,

$$x_{Sm} = \left(B - mH_{eff}^{*}\right) \Big/ H_{tr} \quad ; \quad C\left(x, f_{Sm}\right) = x \sum_{N=0}^{\infty} \frac{p_N^3\left(f_{Sm}\right)}{1 - p_N\left(f_{Sm}\right)}$$

$$p_N\left(f_{Sm}\right) = y \int_0^{\infty} \exp\left(-y f_{Sm} t - t^2 \big/ 2\right) L_N\left(t^2\right) dt \quad ; \quad y = \left(2 \Big/ |x|^{1/2} \right)$$

$$f_{1\pm1} = \left[1 + \left(H_\phi + H_{so}^{*}\right) \big/ H_{tr}\right] ; \; f_{00} = \left[1 + H_\phi / H_{tr}\right] ; \; f_{10} = \left[1 + \left(H_\phi + 2H_{so}^{*}\right) \big/ H_{tr}\right]$$

Here $L_N\left(z\right)$ are Laguerre polynomials. The fitting parameters for this model are shown in equation 2.11.

$$\begin{aligned} H_{eff}^{*} &= 2\left(\alpha^2 - \left(\gamma \left\langle k_z^2 \right\rangle\right)^2 + 2\pi n \alpha \gamma - \pi^2 \gamma^2 n^2 \right) m^{*} \Big/ e\hbar^3 \\ H_{so}^{*} &= \frac{1}{36} \pi^2 m^{*2} n^2 \gamma^2 \big/ e\hbar^3 \end{aligned} \qquad 2.11$$

In here n is the carrier density of the 2DEG. Both Rashba and Dressulhaus spin-orbit coupling constants can be extracted from these two fitting parameters.In the analysis section on chapter 5 of this thesis I only use equation 2.9 to evaluate the magnetoconductance data in the diffusive regime.

Chapter 3

Material system

3.1 Introduction

InSb has the smallest electron effective mass and the largest electron Lande g-factor of all the III-V semiconductors. These properties have long made InSb a promising material for fast switching field-effect transistors [22, 23], sensitive magnetoresistors [24] and ballistic transport devices, however, the large spin-orbit effects predicted for InSb heterostructures have been largely overlooked and make InSb additionally interesting for spintronic applications [25,26].

3.2 InSb quantum well structure

Growth of InSb quantum wells on lattice matched InSb substrates is not feasible for device applications due to the small InSb band gap, which results in a large intrinsic carrier concentration at room temperature [27]. The most appropriate practical option is to grow InSb heterostructures on lattice mismatched semi-insulating substrates like GaAs. The molecular beam epitaxy (MBE) group at University of Oklahoma has done a remarkable job in growing these types of structures for both low temperature (s-series) and room temperature (t-series) device applications [28]. The layer structure of a typical s-series quantum well structure is shown in figure 3.1, depending on the nature of application, the structures have been doped symmetrically or asymmetrically using silicon (Si) δ-doped layers.

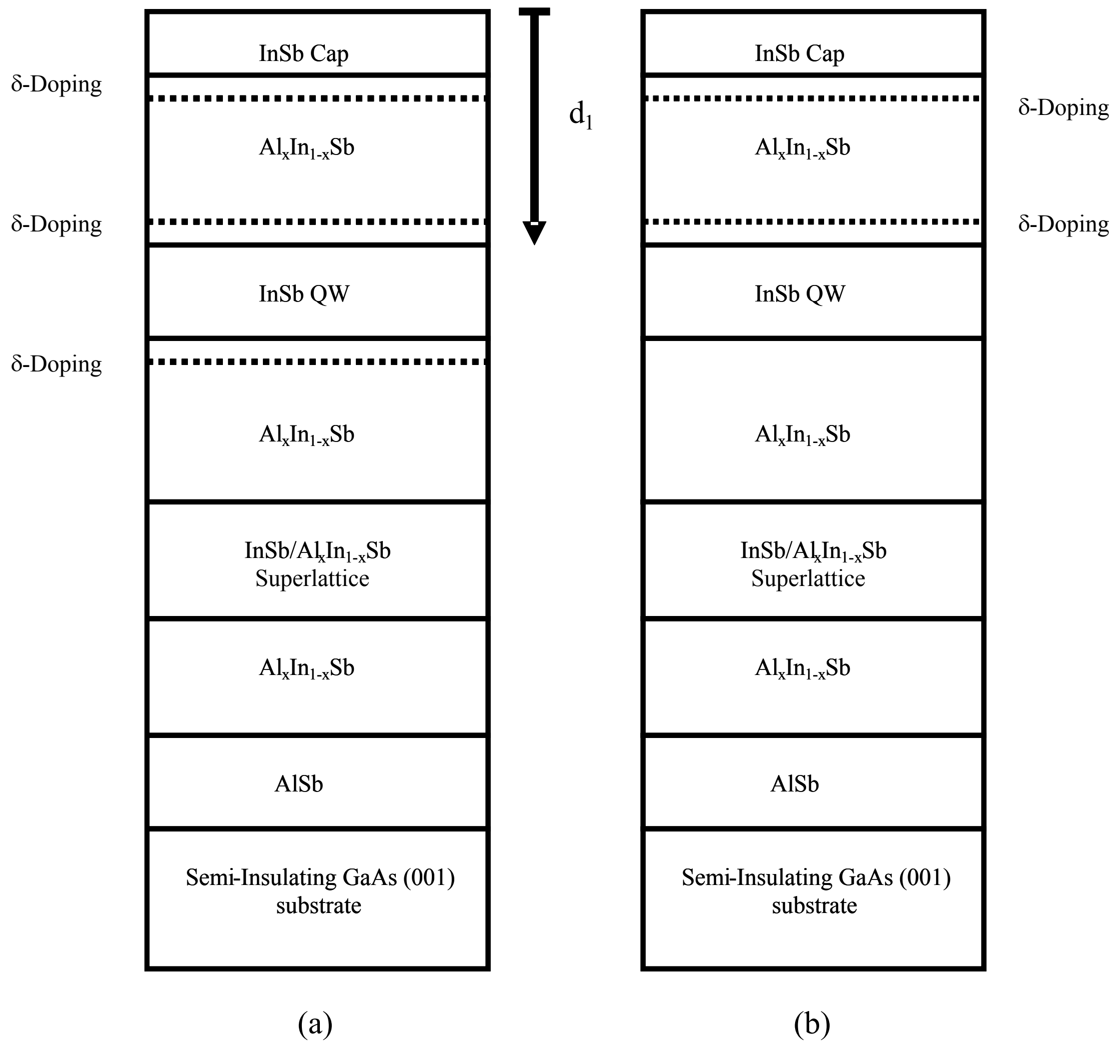

Figure 3.1 Schematic of s-series sample structure (not to scale) (a) symmetrically doped and (b) asymmetrically doped

The typical s-series structures starts with a GaAs (001) substrate. Because of the lattice mismatch of 14.6% between InSb and GaAs the growth initiates with a nucleation layer of AlSb followed by a thick relaxed layer of $Al_xIn_{1-x}Sb$. Further filtering of dislocations is achieved by the strained $InSb/Al_xIn_{1-x}Sb$ superlattice layer. The quantum well itself is sandwiched in between two $Al_xIn_{1-x}Sb$ layers where the x percentage varies from 9% to

15%. The well width ranges from 20 nm to 30 nm to stay below the critical strain relaxation limit of the InSb layer. For symmetrically doped structures, carriers are supplied by two equally spaced Si δ-doping layers on either side of the quantum well and for asymmetric structures, carriers to the well are supplied through a single Si δ-doping layer on top of the quantum well. The additional Si δ-doped layer near the surface is to provide electrons to surface states. The topmost InSb cap layer prevents oxidation of the underlying $Al_xIn_{1-x}Sb$ layer. For s-series samples, the quantum well is typically located at a distance d_1 (150 nm) below the top surface. Further details of growth structure for s-series structures can be obtained from reference 29 and 30.

Key modifications have been adopted in the t-series layer structures (Figure 3.2) to improve defect filtering and quantum confinement. The structure starts with a GaAs (100) substrate cut 2° off toward <110>, to enhance the reduction of micro-twin defect density in the epilayers. The growth initiates with alternating $Al_{0.1}In_{0.9}Sb$ and $Al_{0.2}In_{0.8}Sb$ layers to minimize defect propagation through the structure. The 20nm quantum well is sandwiched in between $Al_{0.2}In_{0.8}Sb$ barrier layers to achieve a higher degree of quantum confinement than the $x_{\max} = 0.15$ s-series well. Like s-series samples, the carriers are supplied by Si δ-doped layers. The structure terminates with an $Al_{0.1}In_{0.9}Sb$ layer and Si δ-doped layer close to the surface to again provide electrons to the surface states traps. The quantum well is located at a distance d_2 (50 nm) below the top surface of the t-series samples which should improve top gating. References 28 and 31 contain further details of the design of t-series structures.

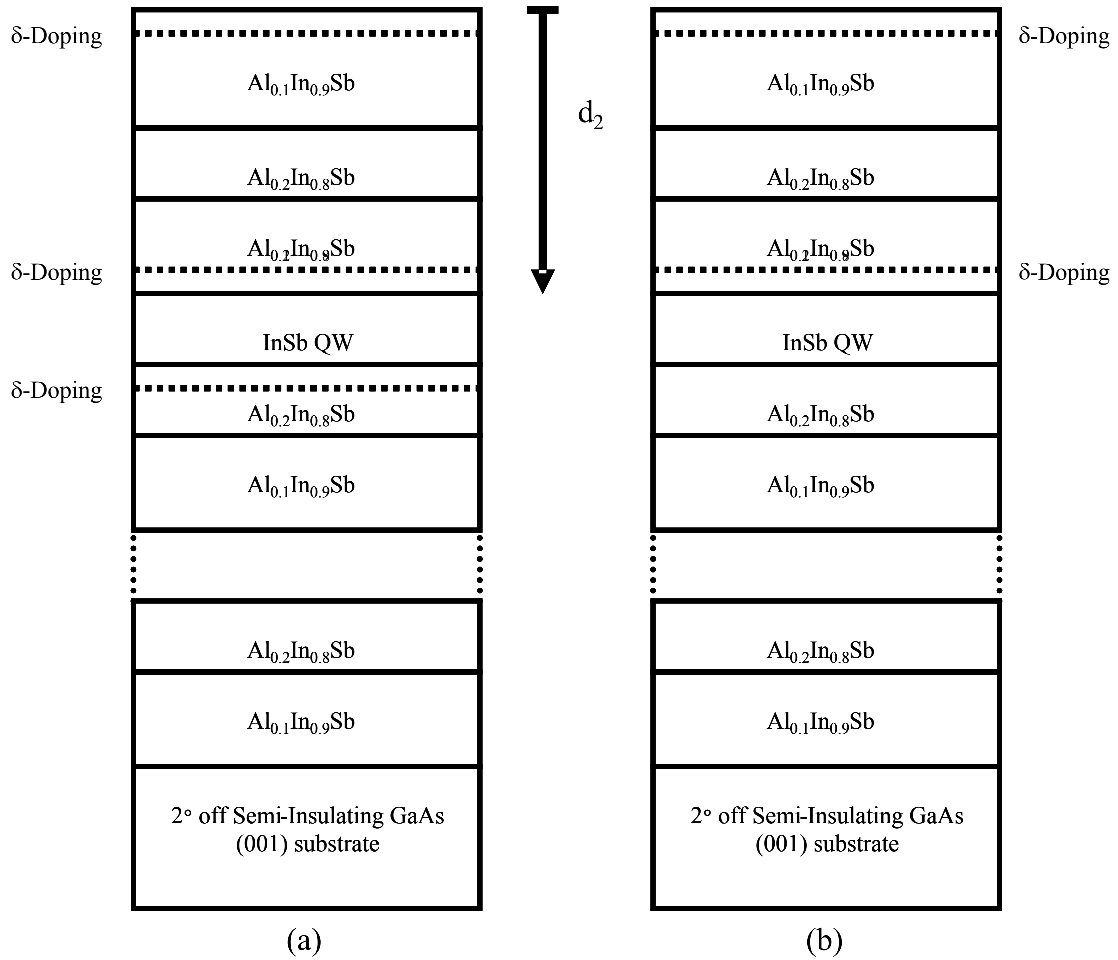

Figure 3.2 Schematic of t-series sample structure (not to scale) (a) symmetrically doped and (b) asymmetrically doped

3.3 Physical properties of InSb

The main focus of this thesis is to investigate the strength of the spin-orbit parameters for InSb. As mention in chapter 1, for quantum wells, the spin-orbit interaction effects arise from the inversion asymmetry of the crystal structure (Dresselhaus effect) and the inversion asymmetry of the as grown structure (Rashba effect). In addition if the crystal

structure is uniaxially deformed, there is a Rashba like SOI due the deformation of the InSb unit cell [19].

In order to evaluate experimental results, it will be important to know the theoretically predicted values for spin-orbit coupling along with some fundamental physical quantities for InSb. In Table 3.1 a comparison has been made for theoretically predicted spin-orbit parameters for InSb with GaAs and InAs along with important fundamental parameters at room temperature.

Property	GaAs	InAs	InSb
Lattice constant $(\AA)$	5.653	6.058	6.479
Band gap energy E_g (eV) at 300 K	1.424	0.354	0.17
Effective mass $\left(m^*/m_e\right)$	0.063	0.023	0.014
S-O gap Δ_0 (eV)	0.34	0.41	0.8
Electron Lande g-factor	-0.44	-17.5	-50.6
Dielectric constant $\left(\varepsilon/\varepsilon_0\right)$	12.9	15.15	16.8
Dresselhaus S-O constant γ $(eV\AA^3)$	27.58	27.18	760.1
Rashba S-O constant α_0 $(e\AA^2)$	5.21	117.1	523.0
Deformation-potential constant C_3 $(eV\AA)$	2.08	6.8	134.5

Table 3.1 Comparison of basic parameters of InSb with other III-V semiconductor materials [27, 32]

Chapter 4

Device fabrication

4.1 Introduction

There are two different experiments covered in this thesis, the first is low field magnetoconductance measurements on $Al_xIn_{1-x}Sb$/InSb quantum wells for weak antilocalization conductance studies and the second part is the study of mescoscopic current focusing devices, more details about these experiments will be discussed in chapters 5 and 6 respectively. The basic building block for both experiments is a standard Hall bar geometry, with additional processing required for current focusing devices. This chapter will cover the various fabrication and measuring techniques which were common to both experiments.

4.2 Photolithography

Standard photolithography was used for Hall bar fabrication. The process starts with cleaving the wafers to match the Hall bar array dimensions on the optical mask. In order to prevent any contamination, processing was done in a class 1000 clean room. Samples undergo a pre-cleaning step of acetone, methanol and isopropanol followed by a dehydration bake at 150°C in a conventional oven before the spin coating process.

Image reversal AZ5214E photoresist was used due to its versatility [33]. A 1.4 μm thick resist layer was deposited on the sample using a spin coater. To achieve the desired thickness, the spin coater operated at 5000 rpm with time duration of 50 seconds. The sample was baked for 60 seconds at 95°C on a hot plate to get rid of excess photoresist

solvents generated during the coating process. Karl Suss MJB3 mask aligner was used to align the sample with the Hall bar mesa pattern using positive photolithography. Ultraviolet (UV) light illuminated the sample through Hall bar photomask pattern for 6.5 sec from a 300W UV source. The pattern was developed for 60 seconds with MIF 319 developer solution followed by a de-ionized water rinse and then blown dry with dry nitrogen gas. A hard bake followed at 120°C for 60 seconds to evaporate any excess solvents from the development process. A schematic of the alignment, exposure and development process is shown in figure 4.1.

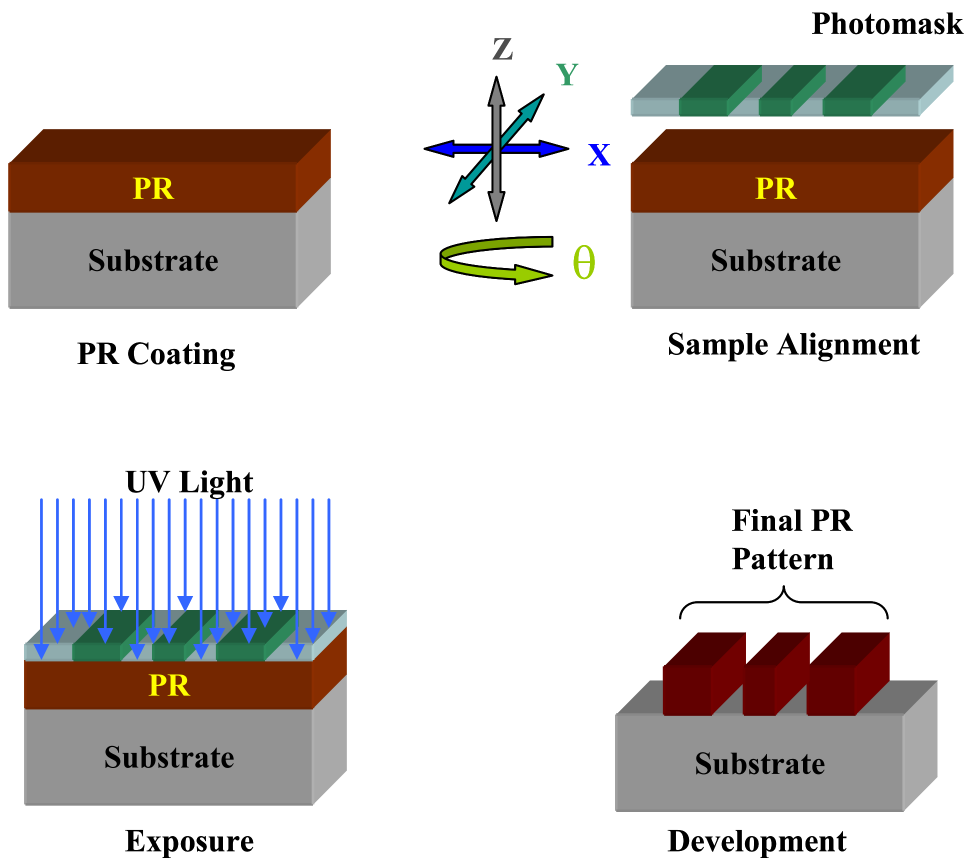

Figure 4.1 Schematic (not to scale) of typical positive photolithography steps

The AZ5214E photoresist has a positive side wall profile for conventional positive photolithography, which is not suitable for liftoff processes. A negative side wall profile is crucial for ohmic contact and gate metal depositions in order to have proper liftoff. The image reversal aspect of AZ5214E can be used to generate negative side wall profiles. The image reversal process is same as for positive lithography up to the initial exposure, after the first 6.5 sec exposure with the resist; the sample undergoes an image reversal bake at 120°C for 60 seconds. During this step the photoresist on the previously exposed area will be cross linked and lose its photosensitivity. A 60 second flood exposure is then done in order to make previously unexposed areas soluble in the developer solution (Appendix A). The rest of the process is same as for positive lithography. The resulting pattern is the inverse of the photomask pattern and the resist walls will now have a negative side wall profile.

4.3 E-beam lithography

The typical minimum feature size which can be patterned with OU's Karl Suss MJB3 is 2 μm. To pattern sub-micron features as in current focusing devices, more sophisticated electron beam lithography has to be employed. The process involves an electron beam scan over a desired surface area coated with an electron beam sensitive film, which is commonly known as e-beam resist. A basic e-beam tool consists of a scanning electron microscope coupled with a computer to control the scan coils to manipulate the electron beam. The capability of high resolution pattern generation, the flexibility to work with a variety of materials and the ability generate an infinite number of patterns are definite

advantages of this technique [34]; nevertheless it a slow, expensive and complicated process. Figure 4.2 shows a schematic of a typical e beam tool.

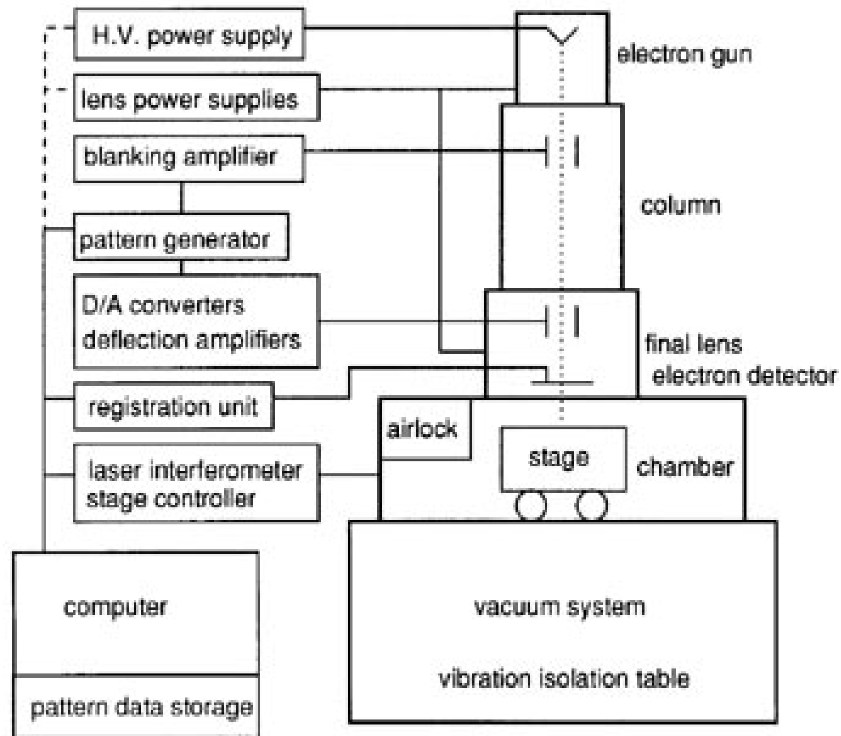

Figure 4.2 Block diagram showing the major components of a typical electron beam lithography system [34]

In modern e-beam tools, computer control of the column scan coils is responsible for forming and controlling the electron beam. Underneath the column is a chamber containing a stage for moving the sample around and which also acts as a load lock for sample loading and unloading. The computer also handles functions such as setting up an exposure job, loading and unloading the sample, aligning and focusing the electron beam, sending pattern data to the pattern generator, electron beam blanking and movement of the sample stage.

We used etch resistive UV113 e-beam resist for e-beam lithography. A 350 nm thick layer of UV113 was deposited on top of the mesa (mesa etching will discussed in section 4.3) using the spin coater, operating at 5000 rpm for 50 second to achieve the desired thickness. The sample was then baked at 150°C for 60 seconds to evaporate any excess resist solvents. Sample patterning was performed on a RAITH 150 e-beam tool with a 30 KV beam and an optimum dose of 28 $\mu C/cm^2$. The sample then has a post exposure bake of 130°C for 90 seconds before development. Samples were developed in DC 265 developer solution for 60 seconds followed by a de-ionized water rinse and then blown dry with dry nitrogen gas (Appendix B).

4.4 Wet etching

In wet etching of semiconductor materials, first the chemical species must be transported to the surface in order to allow chemical species adsorption. Chemical reactions then occur at the surface and the reaction byproducts are released and move away from the surface [35]. The basic mechanism of semiconductor wet etching involves formation of oxides on the top surface using a strong oxidizer and dissolving them by means of either an acid or base.

For $InSb/Al_xIn_{1-x}Sb$ quantum well structures, the photolithographically patterned Hall bar mesas were etched using a HF base solution made from 6 parts 3% H_2O_2, 3 parts 2.5% HF and 1 part 85% lactic acid. For this solution, the etch rate is 1.3 μm/min. For better control of desired etch depths, 1 part of this solution was diluted with 3 parts of de-ionized water. The resulting etch rate is 0.82μm/min. The samples were etched 100 nm below the last δ-doped layer to prevent any parallel conduction at low temperatures. After

etching the sample for the appropriate time, the etching process can be stopped by immersing the sample in de-ionized water for two minutes followed by drying with dry nitrogen gas. The protective AZ5214E resist layer on top of Hall bar area can be removed with Shipley 1165 photoresist remover. Due to the isotropic nature of wet chemical etching the horizontal device dimensions must be greater than the desired etch depth; therefore wet etching is not suitable for sub-micron size feature isolation [36].

4.5 Reactive Ion Etching (RIE)

Reactive ion etching enables high resolution, anisotropic pattern transfer which is a key requirement for sub micron size feature isolation. Reactive ion etching can be categorized in the four basic processes as shown in figure 4.3 [37].

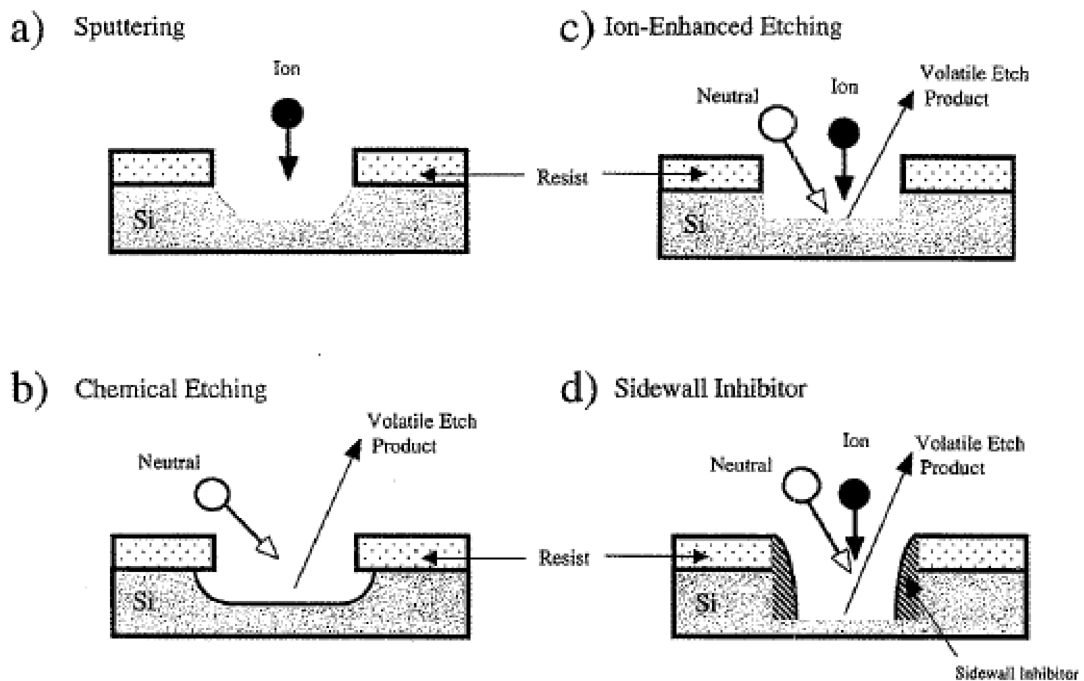

Figure 4.3 schematic diagram of (a) sputtering, (b) chemical, (c) ion-enhanced, and (d) sidewall inhibitor etch mechanisms

(i) Physical sputtering

Accelerated ions transfer large amount of energy (>100eV) and momentum to the semiconductor surface causing mechanical removal of material. This process causes significant surface damage and has low chemical selectivity.

(ii) Chemical etching

This process is quite similar to wet chemical etching. The only difference is the plasma medium in which the reactions take place. This process involves mostly reactive neutral gas species which produce volatile etch products. Due to the low level of ion bombardment, the plasma induced damage is minimal, however the etch profile tends to be isotropic.

(iii) Ion-enhanced etching

Both physical and chemical etching occurs during this process. Anisotropic etch profiles can be obtained due the directional nature of ions accelerated through the plasma to the semiconductor surface. Energetic ions also assist in the removal of volatile etch products.

(iv) Sidewall inhibitor etching.

For this process, a polymer forming gas is added to the chamber to initiate the formation of a thin layer on the side walls of the etch profile to prevent lateral etching.

4.5.1 High density inductively coupled plasma (ICP)

As mentioned in chapter 2 for InSb/$Al_xIn_{1-x}Sb$ quantum well structures, the quantum well itself is located very close the surface. Therefore it is essential that relatively low ion bombardment is used during the etching process in order to minimize ion induced

damage. On the other hand lowering the ion energy will reduce the etch rate. Thus to keep the etch rate high, it is important to increase the ion flux [36]. The etch rate only depends on the ion power incident on the sample.

The ion flux can be increased by using a high density inductively coupled plasma system. A schematic of an ICP system is shown in figure 4.4 [37]. The plasma is formed in a dielectric chamber which has an inductive coil around it. Radio frequency (RF) power applied to this coil will generate an electric filed in the horizontal plane. This results a strong magnetic field in the vertical plane confining both electrons and ions in the plasma at the center of chamber generating a high plasma density.

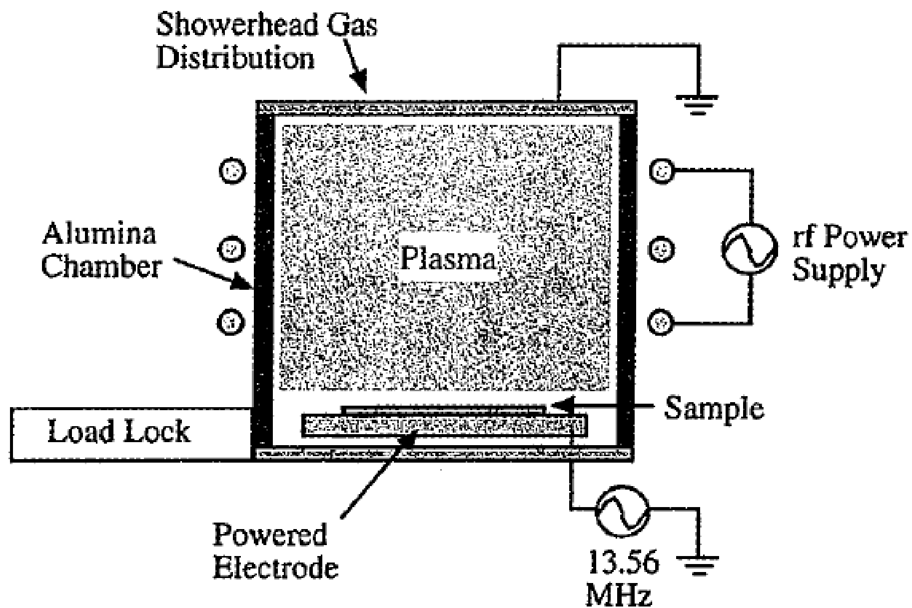

Figure 4.4 Schematic diagram of inductively coupled plasma (ICP) etch system

4.5.2 Etching of InSb with $CH_4/H_2/Ar$ based plasma

CH_4/H_2 based plasma etching has been widely used for III-V semiconductor material etching [38,39,40,41] which provides isotropic etching with vertical side wall profiles. The process starts with plasma formation due to ionization of CH_4, H_2 and Ar. Since the

dissociation potential is only 4.6 eV for $CH_4 + e \rightarrow CH_3 + H + e$, reactive species of CH_3 and H can be easily generated. The precursor H_2 contributes to etching in two ways, one is by providing an alternate source of H and the other is as a diluting medium for the CH_4 plasma. The latter contribution is critical because a high CH_4 concentration causes a byproduct polymer deposition on the sample surface and the RIE chamber. An additional Ar precursor enhances the ionization and aids in the removal of polymers by means of physical sputtering. During the etching process, volatile products such as $In\left(CH_3\right)_3$ and SbH_3 will be generated, however CH_3-based products are less volatile than H-based products resulting in preferential loss of Sb from the surface.

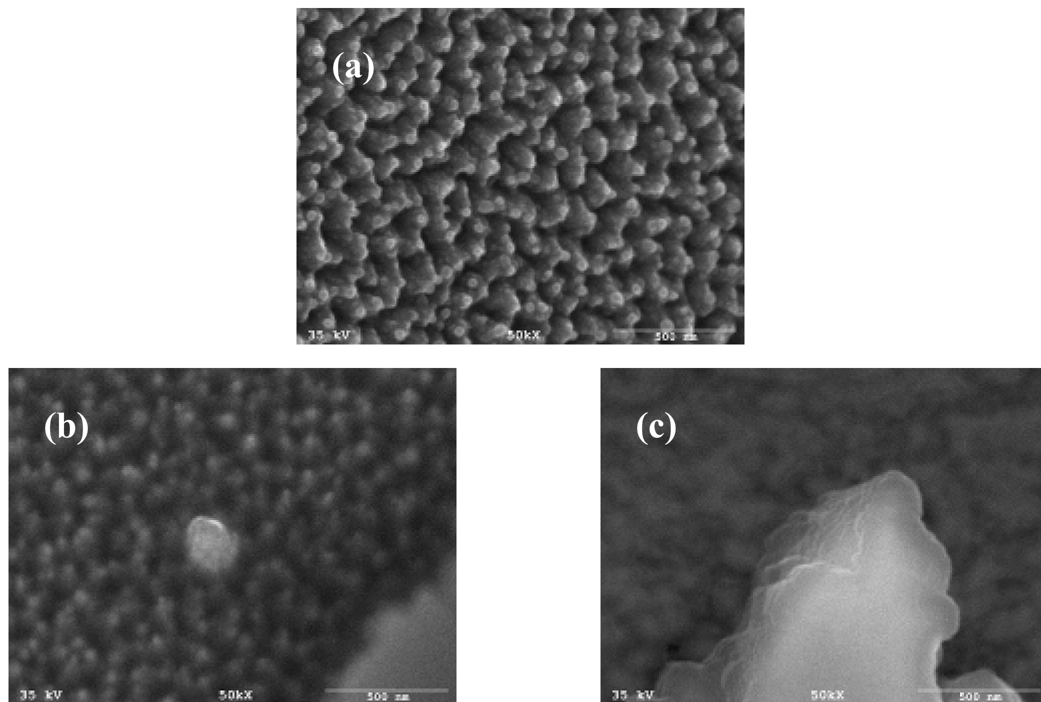

Figure 4.5 SEM micrographs of InSb samples etched with $CH_4/H_2/Ar$ RIE with CH_4/H_2 ratio of (a) 15.8%, (b) 30%, (c) 70%

In InSb/$Al_xIn_{1-x}Sb$ systems we use $CH_4/H_2/Ar$ gas mixtures use to physically isolate 2DEGs with submicron trenches. The total gas flow rate and Ar flow rate were kept constant at 30 sccms and 8 sccms respectively while changing the $CH_4:H_2$ ratio to 15.8%, 30% and 70% for different trenches. Both RIE and ICP powers were set to 75 W and the process was performed at a pressure of 10 mTorr for 20 minutes. As shown in SEM micrographs in figure 4.5 the lower CH_4/H_2 ratio trial resulted in In-rich rough surfaces while for higher ratios of CH_4/H_2 led to excessive polymer deposition. The resulting maximum etch rate was 100 Å/min which corresponds to a CH_4/H_2 ratio of 15.8% (Appendix C), however the unwanted polymer that was deposited created problems in removing the e-beam resist from the sample thus hindering additional processing.

4.5.3 Etching of InSb with BCl_3/Ar Based plasma

Due to the low etch rate, polymerization and rough surface morphologies associated with CH_4/H_2 based RIE on InSb/$Al_xIn_{1-x}Sb$ semiconductor heterostructures, we also used BCl_3 based RIE. BCl_3 RIE is known for its immediate removal of the native oxide on the surface and also as a getter for water vapor within the reactor chamber [44].

BCl_3/Ar plasma was used to etch Insb/$Al_xIn_{1-x}Sb$ heterostructure trenches. The flow rate ratio of BCl_3: Ar was kept constant (1:4) and the RF power varied while setting the ICP power to zero. This process was performed at room temperature with 3mTorr chamber pressure for 200 seconds. As shown in the SEM micrographs of Figure 4.6, the trenches were covered with a solid material.

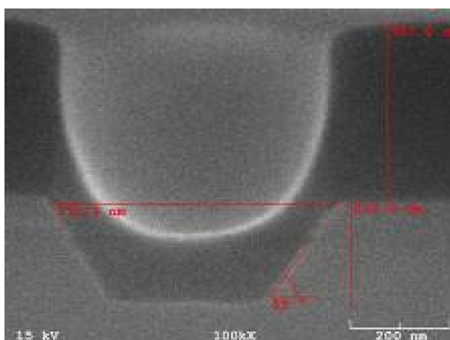

Figure 4.6 Solid material formation after RIE (RF power = 120W)

This is due to higher melting points of In-chloride etch products compared to Al and Sb chloride products which results in a tendency for it to remain on the etch surface. Relevant boiling points are: InCl = 608 °C; $InCl_2$ = 560 °C; $InCl_3$ = 600°C [45], however even with the InCl deposition the etch rate is superior to the CH_4/H_2 based RIE. The graph in Figure 4.7 indicates that even without any ICP power an etch rate of 320 Å/min can be achieved with 75W RF power.

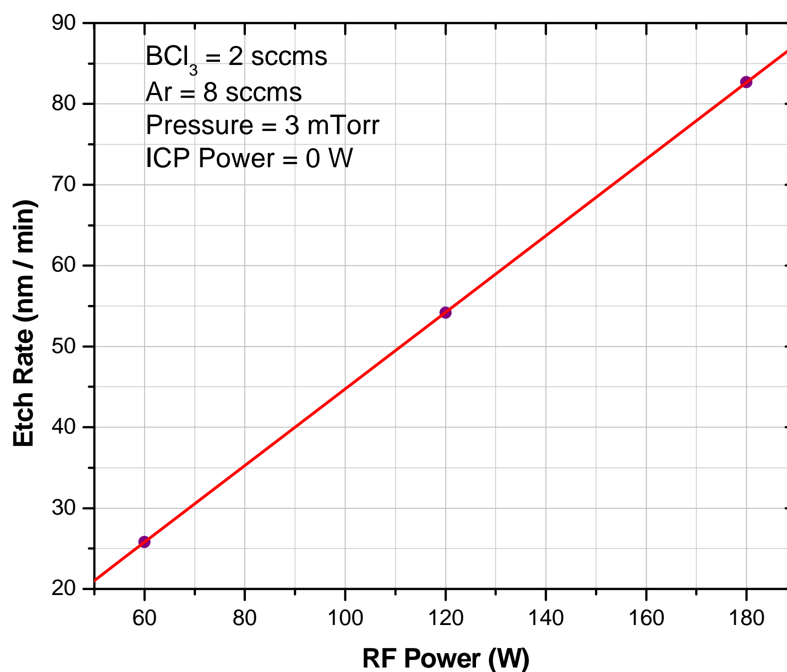

Figure 4.7 RIE etch rate vs. RF power

At higher RF bias the etched trenches show an asymmetry which may have been caused by a lack of plasma directionality from the ICP source. SEM micrographs in Figure 4.8 clearly show the lack of symmetry of etched trenches at higher RF power settings.

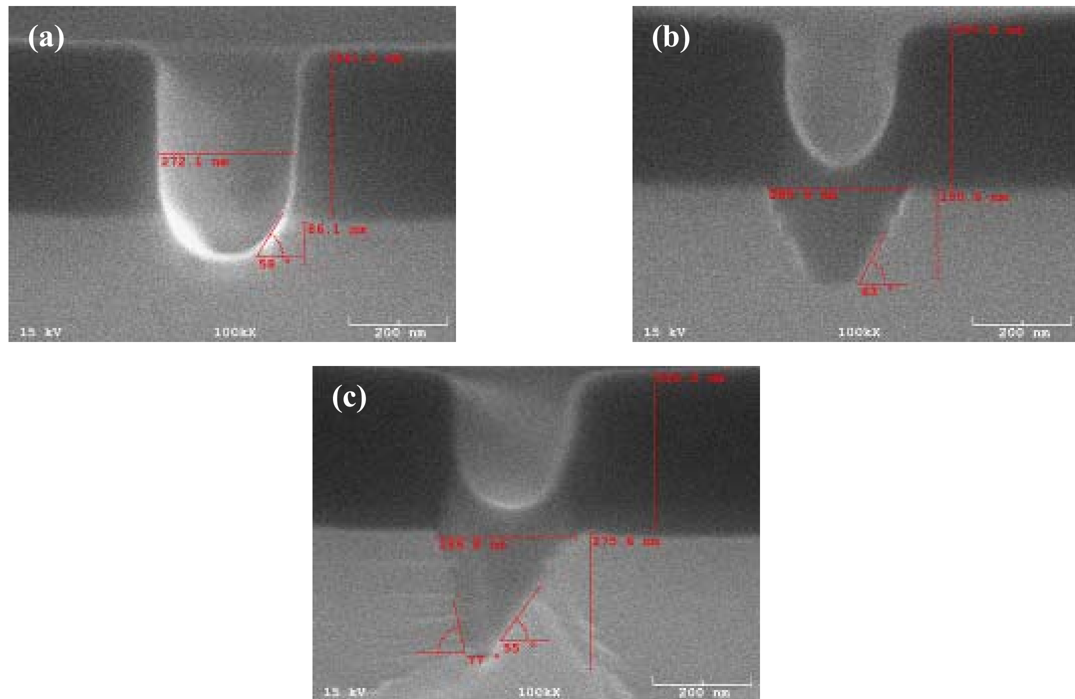

Figure 4.8 SEM micrographs of InSb samples etched with BCl_3/Ar RIE with BCl_3 = 2 sccms, Ar = 8 sccms and ICP Power = 0W (a) RF Power = 60W, (b) RF Power = 120W (c) RF Power = 180W

The optimized recipe has a 67° side wall angle. It was achieved for an ICP power of 50 W, RF power of 100 W and BCl_3 and Ar flow rates of 3 sccms and 12 sccms, respectively, with a total pressure of 3 mTorr (Appendix C). Figure 4.9 indicates the side wall profile of a 200nm etched trench.

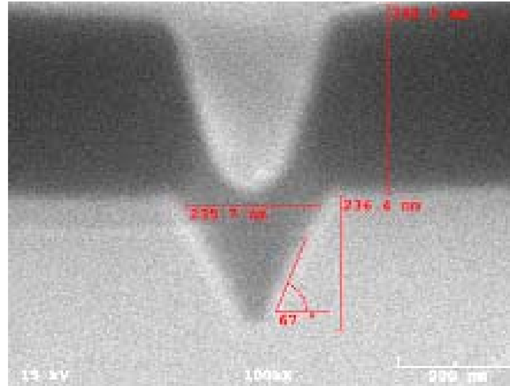

Figure 4.9 SEM micrograph of 200 nm RIE trench with the optimized recipe

4.6 Ohmic contacts, deposition and annealing

Satisfactory ohmic contacts for n-type $InSb/Al_xIn_{1-x}Sb$ heterostructures are often provided by Indium [46]. After Hall bar mesa fabrication, another photolithography step was performed for contacts. An Edwards model E306A vacuum coating system was used to thermally evaporate Indium on Hall bar contact pads. The thickness of the deposited Indium layer is measured by a quartz crystal monitor. The crystal monitor reading for a typical Indium evaporation was around 700 nm. Profilometer measurements on witness samples indicate a tooling factor of 0.5 for Indium, which corresponding to an actual thickness of 350 nm.Samples were annealed at 230 °C for 5 minutes in a forming gas environment (N_2-80%, H_2-20%) to diffuse the deposited Indium into the quantum well.

4.7 Sample mounting and wire bonding

After all the relevant fabrication steps were performed on an array of Hall bars, the array has to be separated. The array was first scribed with the aid of alignment markers on the wafer using a Tempress-1713 manual scriber. Before making scriber marks the tool

height has to be adjusted to match the sample thickness. After scribing, a home built cleaving station was used to cleave the sample into individual Hall bars without damaging the mesa and contacts. See figure 4.10.

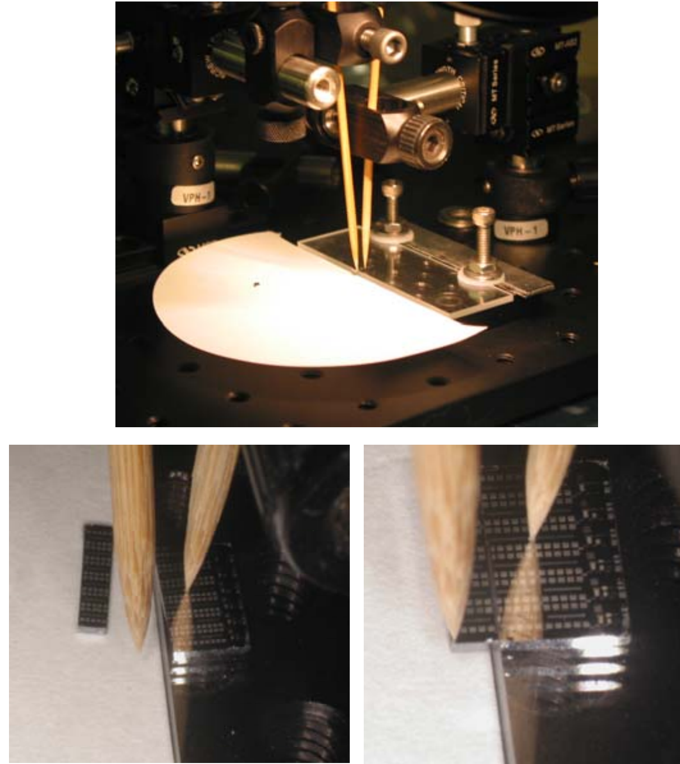

Figure 4.10 Schematic of sample cleaving steps

The Hall bars were then mounted on a 28-pin plastic leaded chip carrier (PLCC-CCJ02803 from Spectrum semiconductor materials INC) with two component EPO-TEK H20E silver epoxy. A curing time of 45 minutes at 120 °C in an oven is required to harden the epoxy. Samples were wire bonded using K&S 4500 digital series manual wedge bonder with high purity 25μm gold wire. Wire bonding was performed in an unconventional manner due to the softness of Indium (Appendix D). The first bond was made on PLCC gold pad and then moved to Indium pad to finish up the bonding cycle. Figure 4.11 shows three Hall bars mounted and wire bonded on a PLCC.

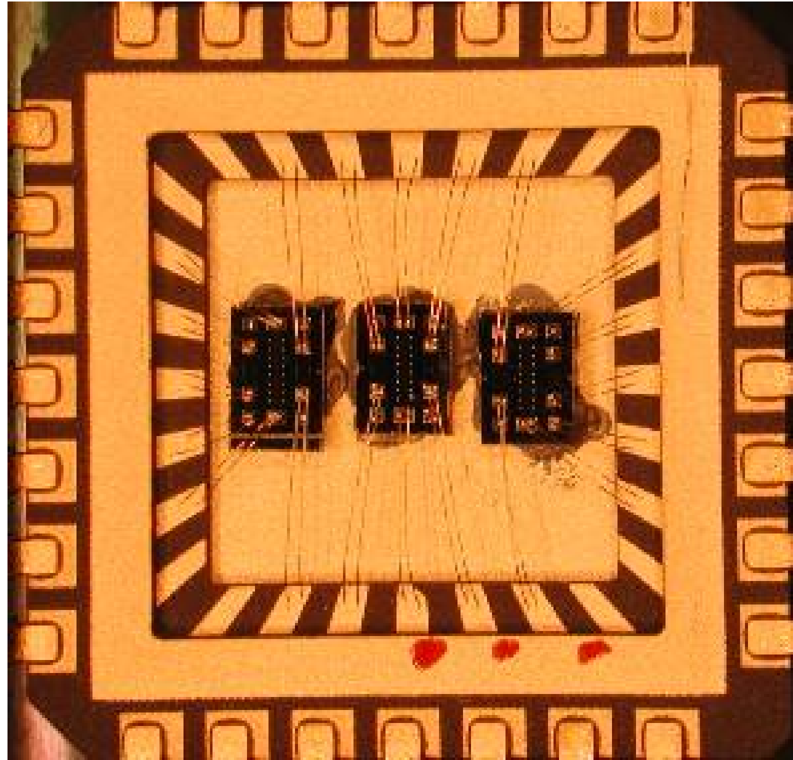

Figure 4.11 28-Pin PLCC with three wire bonded Hall bars

4.8 Sample thin down

For back gating the samples were thinned down to 100 μm from the back side. The sample is first mounted on a polishing plate using crystalbond-509 wax. The initial thin down to ~500 μm was performed by 2500 grit size sandpaper paper using a lapping and polishing machine. Diamond polishing papers with grit sizes varying from 50 μm to 10 μm were used to thin down the samples from 500 μm to 100 μm. Finally the sample was carefully removed from the polishing plate by soaking the assembly in Acetone for 20 minutes. Thermal evaporation was used to deposit chromium and gold metal layers for the back gates.

4.9 Low temperature magnetotransport measurements

Low temperature magnetoconductance measurements were obtained using a home built ^{3}He cryostat. The superconducting magnet can generate a maximum field of 9T at 4.2K. Four-terminal electrical measurements were taken using standard AC lock-in measurements by a Stanford SRS 830 lock-in amplifier as well as by a Linear Research LR 700 AC resistance bridge. Low noise measurements were made by with a 100 nA current with a frequency of 13 Hz and measuring the voltage difference between desired voltage probes.

Chapter 5

Weak antilocalization in InSb Quantum wells

5.1 Introduction

Although weak antilocalization has been observed previously for heterostructure systems such as GaAs/AlGaAs [5,21,47,48], InP/GaInAs [49,50], and GaN/AlGaN [51,52], to the author's best knowledge there has not been any complete investigation of weak antilocalization on InSb/AlInSb heterostructures. This chapter details experimental investigations of weak antilocalization in InSb/AlInSb Hall bars along with the relevant theoretical interpretation of characteristic length/time scales and the strengths of spin-orbit coupling parameters.

5.2 Temperature dependence of weak antilocalization

Hall bar samples from wafers t162 and t256 have been used to analyze the temperature dependence of weak antilocalization in InSb/AlInSb heterostructures. Both wafers were grown with asymmetric doping. Details of the sample structures including mobility and density at 4.2 K are listed in table 5.1.

Sample ID	Al%	Well Width (Å)	Carrier Density (n_s) at 4.2 K (cm^{-2})	Mobility (μ) at 4.2 K(cm^2/V.Sce)
t162	20	250	3.34×10^{11}	102000
t265	20	200	2.24×10^{11}	43000

Table 5.1 Sample parameters for InSb/AlInSb heterostructures

During the experiment, longitudinal magnetoresistance measurements were made to capture the resistance peak which signifies the weak antilocalization. The resistance data is then converted into longitudinal resistivity by using $\rho_{xx} = R_{xx}\frac{W}{L}$ where R_{xx} the measured longitudinal resistance, W is the width of the Hall bar and L is the distance between the two voltage probes. The magnetoconductivity data were obtained by taking the inverse of ρ_{xx} and normalizing by the factor $e^2/\pi h$. The temperature dependence of the weak antilocalization signals for samples t162 and t265 for temperatures ranging from 10 K to 1.5 K are shown in Figure 5.1 and Figure 5.2, where the conductivity correction $\sigma(B)-\sigma(B=0)$ is provided versus magnetic field.

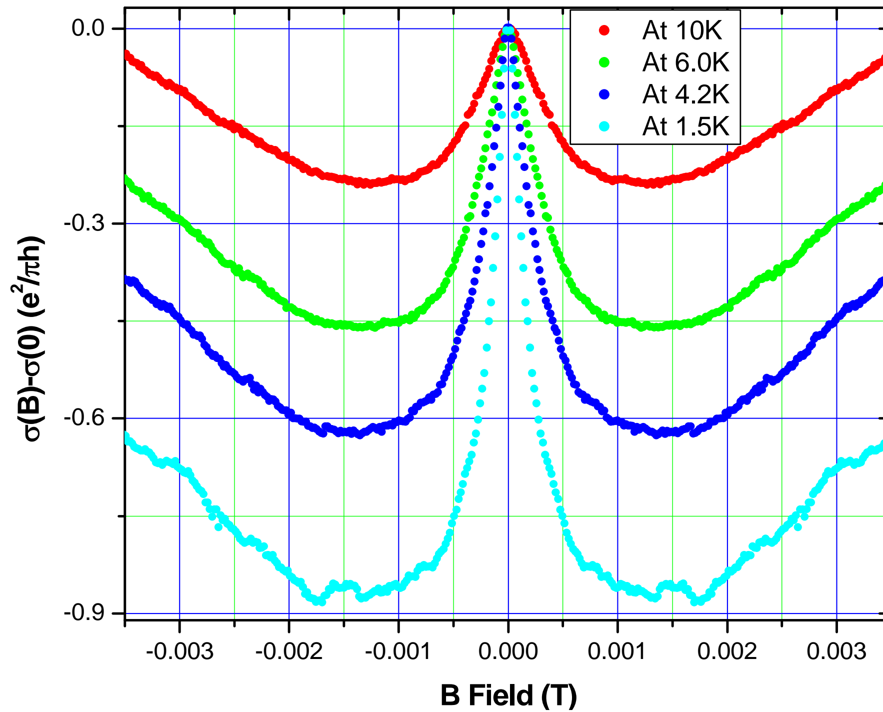

Figure 5.1 Experimental magnetoconductivity $\sigma(B)-\sigma(0)$ of sample t162 for different temperatures

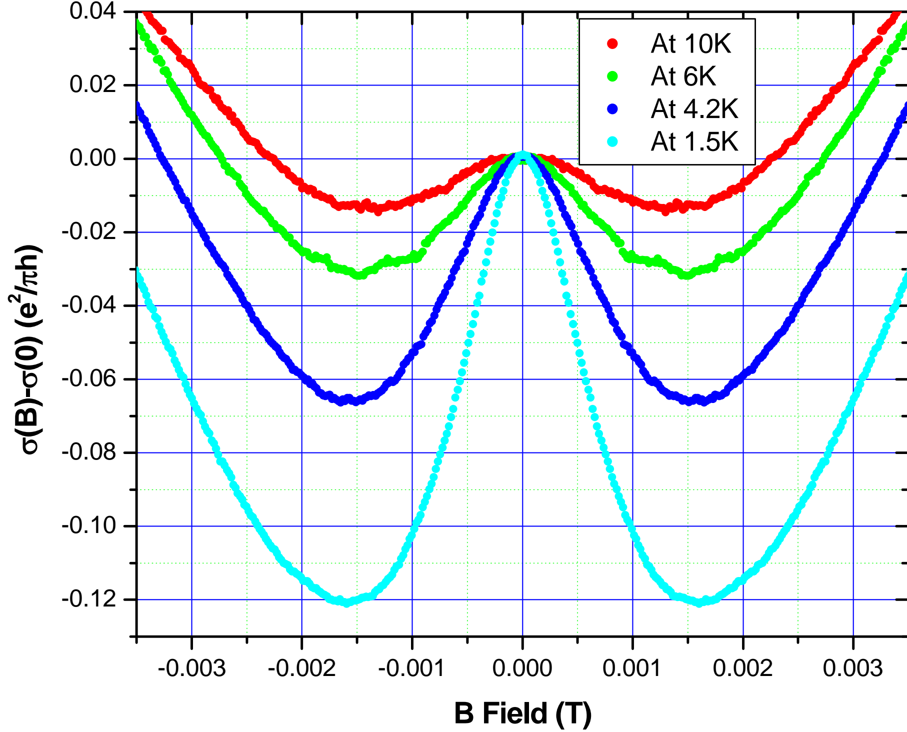

Figure 5.2 Experimental magnetoconductivity $\sigma(B)-\sigma(0)$ of sample t265 for different temperatures

The large conductivity correction for t162 compared to t256 results from the density dependence of the phase breaking length l_ϕ as will be shown [51, 52]. HLN theoretical fittings to the experimental data have been performed up to $B = B_{tr}$ which is appropriate for the weak antilocalization conductivity correction in the diffusive regime [17]. The two fitting parameters $\left(H_{so}, H_\phi\right)$ program was written in Mathematica version 6.0. The program uses experimentally obtained magnetoconductance data and initial values for H_{so} and H_ϕ as input parameters. To estimate the best fitting parameters, the built-in nonlinear regression function was used.

The relevant length and times scales extracted from fittings using equations 5.1 are shown in table 5.2.

$$\tau_{so} = \frac{\hbar}{4eDH_{so}}; \quad l_{so} = \left[\frac{\hbar}{4eH_{so}}\right]^{1/2}$$
$$\tau_{\phi} = \frac{\hbar}{4eDH_{\phi}}; \quad l_{\phi} = \left[\frac{\hbar}{4eH_{\phi}}\right]^{1/2} \qquad 5.1$$

For both samples the extracted spin orbit time remains roughly constant over the considered temperature range while the phase breaking rate $1/\tau_{\phi}$ has linear temperature dependence as shown in figure 5.3.

Sample ID	Temperature (K)	Phase breaking length l_{ϕ} (μm)	Phase breaking time τ_{ϕ} (psec)	Spin orbit length l_{so} (μm)	Spin orbit time τ_{so} (psec)
t162	10	1.29	3.1	0.821	1.24
	6	1.70	5.3	0.80	1.18
	4.2	1.94	6.9	0.79	1.15
	1.5	2.7	14	0.84	1.4
t265	10	0.56	1.89	0.56	1.88
	6	0.65	2.53	0.58	2.03
	4.2	0.77	3.53	0.60	2.16
	1.5	0.92	5.05	0.62	2.27

Table 5.2 Important length and time scales obtained from HLN fittings for different temperatures

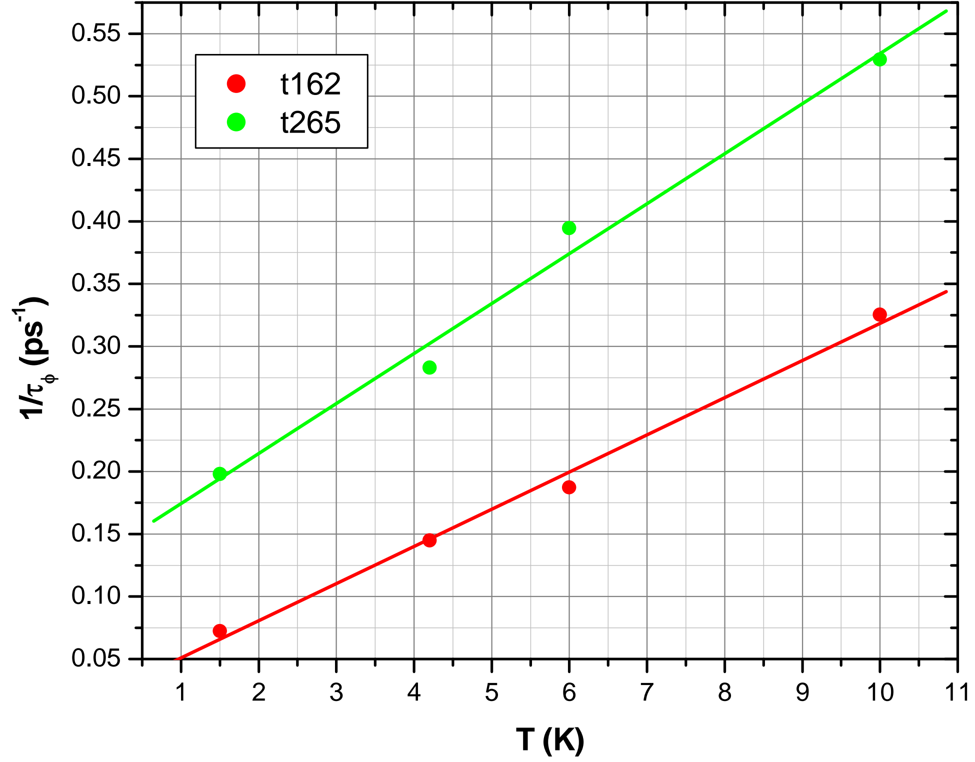

Figure 5.3 Phase breaking rate as a function of temperature for sample t162 and t265

At low temperatures where the electron-electron interaction is the dominant temperature dependent inelastic scattering mechanism, the temperature dependence of the phase coherence rate is given by [53, 54, 55].

$$1/\tau_\phi = \begin{cases} \frac{\pi}{2}\frac{(k_B T)^2}{\hbar E_F}\ln\frac{E_F}{k_B T}, \text{ when } T > \frac{\hbar}{k_B \tau_{tr}} \\ \frac{k_B T}{2\pi N_0 D\hbar^2}\ln(\pi D N_0 \hbar), \text{ when } T < \frac{\hbar}{k_B \tau_{tr}} \end{cases} \qquad 5.2$$

where $N_0 = m^*/\pi\hbar^2$ is the 2D density of states. The observed T dependence suggests that we are in the $T < \frac{\hbar}{k_B \tau_{tr}}$ range. For t162 the factor $\frac{\hbar}{k_B \tau_{tr}}$ is 8.8 K and for t265 it is 20.9K.

The temperature ranges considered thus generally satisfy the inequality $T < \frac{\hbar}{k_B \tau_{tr}}$.

According to equation 5.2 the phase de-coherence rate with calculated prefactor to the linear term should be,

$$1/\tau_\phi = \begin{cases} 3.860\times10^{-3}(p\sec^{-1}K^{-1})\,T & for\ t162 \\ 9.269\times10^{-3}(p\sec^{-1}K^{-1})\,T & for\ t265 \end{cases} \qquad 5.3$$

However the linear relationship extracted from fits to the data in figure 5.3 have the following form.

$$1/\tau_\phi = \begin{cases} 2.973\times10^{-2}(p\sec^{-1}K^{-1})\,T + 2.118\mathrm{X}10^{-2}(p\sec^{-1}) & for\ t162 \\ 3.997\times10^{-2}(p\sec^{-1}K^{-1})\,T + 1.344\mathrm{X}10^{-1}(p\sec^{-1}) & for\ t265 \end{cases} \qquad 5.4$$

The fits not only take into account the temperature dependence of $1/\tau_\phi$ but also the zero temperature limit where the intrinsic scattering rate is dominated by electron-impurity scattering, which is inversely proportional to mobility and temperature independent. As can be seen for sample t162, the temperature dependence of the phase breaking rate is a factor of 7.7 larger than theoretically predicted whereas for sample t265 the factor is 4.3. A factor of 4 difference has been reported for weak antilocalization measurements on p-type $Al_xGa_{1-x}As/GaAs$ heterostructures [56]. For the theoretical predictions an electron effective mass of $0.015m_e$ was used. A number of facts may be responsible to explain this discrepancy: we may be in a crossover regime between the T and T^2 dependence, and the non-parabolicity of the conduction band may contribute to a larger effective mass m^* than that used in the calculation [56].

5.3 Gate voltage dependence of WAL for asymmetric samples

Unlike silicon, which possesses a high quality native oxide, thermally grown oxides on III-V materials have poor performance in top gating applications. Also deposition of insulating materials is quite difficult because of the existence of a nominally 3 nm thick native oxide layer with a high concentration of interface states [57]. These interface states screen the semiconductor by pinning the Fermi level in the conduction band. Due to these difficulties we have used back gating to control the carrier density.

As mentioned in chapter 4 samples were thinned down to 100 μm from the back side and polished for metal gate deposition. Sample t134 was selected for back gating because of its moderate carrier concentration of 3.61×10^{11} cm^{-2} at 4.2 K. This is an asymmetrically doped structure with a 20 nm quantum well and $Al_{0.2}In_{0.8}Sb$ barrier layers. Back gate voltages varying from -20V to +20V were applied to the Hall bar resulting in a linear density change as shown in figure 5.4.

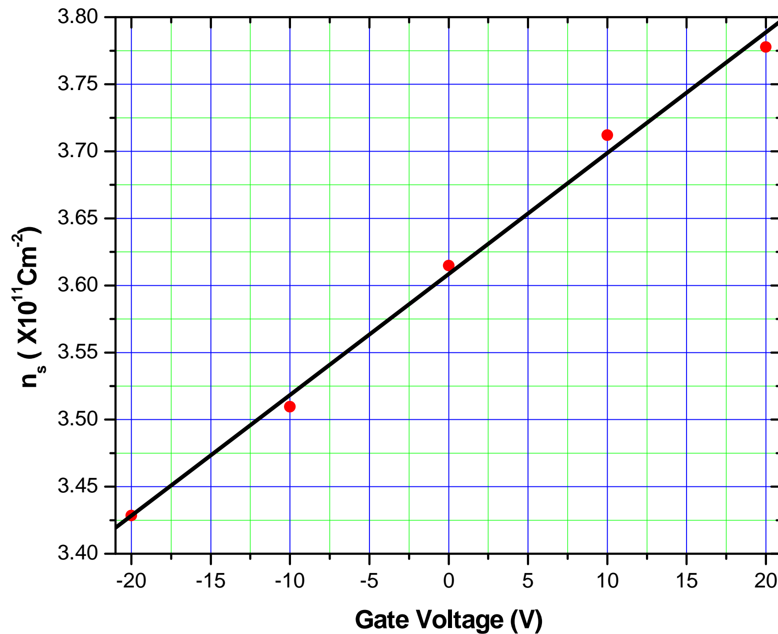

Figure 5.4 Electron densities as a function of back gate voltage for sample t134

Although the change in carrier density was small (~10%), the weak antilocalization signal changed significantly as shown in figure 5.5. The change in the location of the conductivity minima is empirical evidence of the change in spin-orbit coupling with the change in carrier density [5, 48]. Under the assumption that the Rashba spin-orbit term dominates in asymmetric structures compared to the Dresselhaus term, the HLN theory can be applied in order to extract spin-orbit parameters [58]. The fits confirm that the sample is in the diffusive transport regime since the phase coherence lengths (l_ϕ) obtained from HLN fittings are a factor of three larger than the mean free path (l_{tr}), and the spin-orbit lengths (l_{so}) are always greater than l_{tr} .

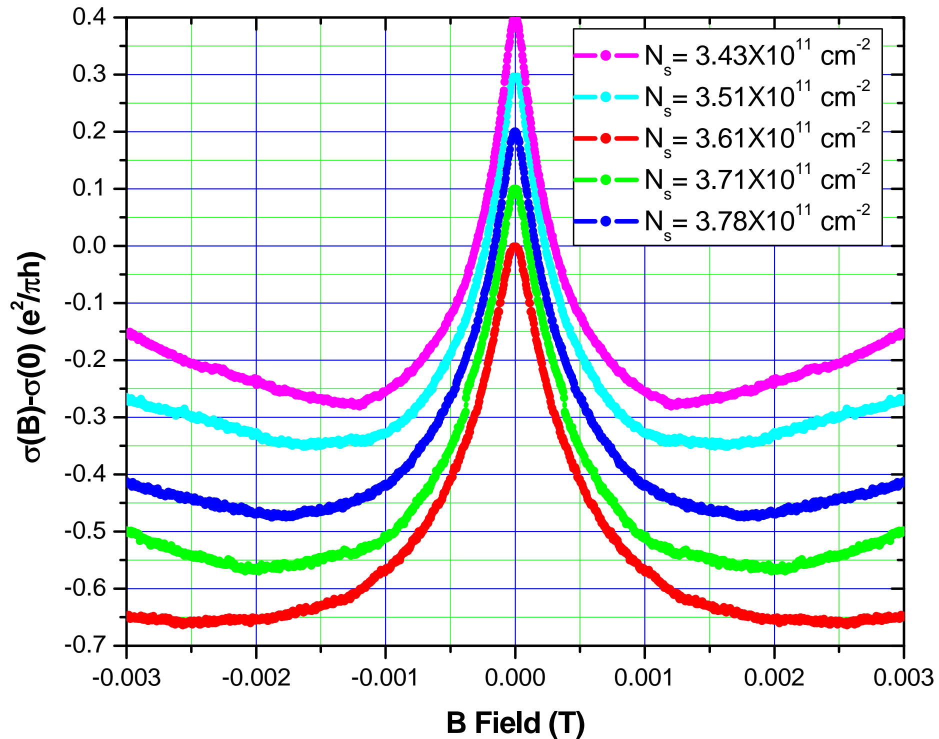

Figure 5.5 Weak antilocalization conductivity correction measured at different carrier densities for sample t134. The curves have been shifted vertically for clarity

Carrier Density, N_s (cm^{-2})	Mobility μ (cm^2/V.sec)	Transport length, l_{tr} (μm)	Spin-orbit length, l_{so} (μm)	Phase breaking length, l_ϕ (μm)
3.43×10^{11}	74000	0.51	0.59	2.00
3.51×10^{11}	76700	0.53	0.64	2.17
3.61×10^{11}	80000	0.56	0.66	2.24
3.71×10^{11}	83000	0.59	0.72	2.38
3.78×10^{11}	85000	0.61	0.73	2.51

Table 5.3 Extracted length scales obtained from HLN fittings for different carrier densities

The extracted spin-orbit lengths and times along with other important transport parameters are summarized in table 5.3. There is similar trend of variation on density for both l_ϕ and l_{so}. The phase breaking length change is due to the changes in both density and mobility while the change in spin orbit length is due to the change in the strength of spin-orbit coupling of the structure with the carrier density alone. The values of l_{so} at different densities are shown in figure 5.6. It is evident that l_{so} has a linear dependence versus the carrier density of the system.

Using the parameters obtained from HLN fitting routines and zero field resistivity measurement values for the Rashba spin precession vector, Ω_R can be calculated. In order to extract effective Rashba spin-orbit coupling constants we calculated the in-plane wave vector at the Fermi energy using the nonparabolic dispersion relation shown in equation 5.5 by putting $E = E_F$ [58]. Other relevant values were obtained from table 3.1 in chapter 3.

$$\hbar^2 k^2 / 2m_0^* = E\left(1 + E / E_g\right) \quad 5.5$$

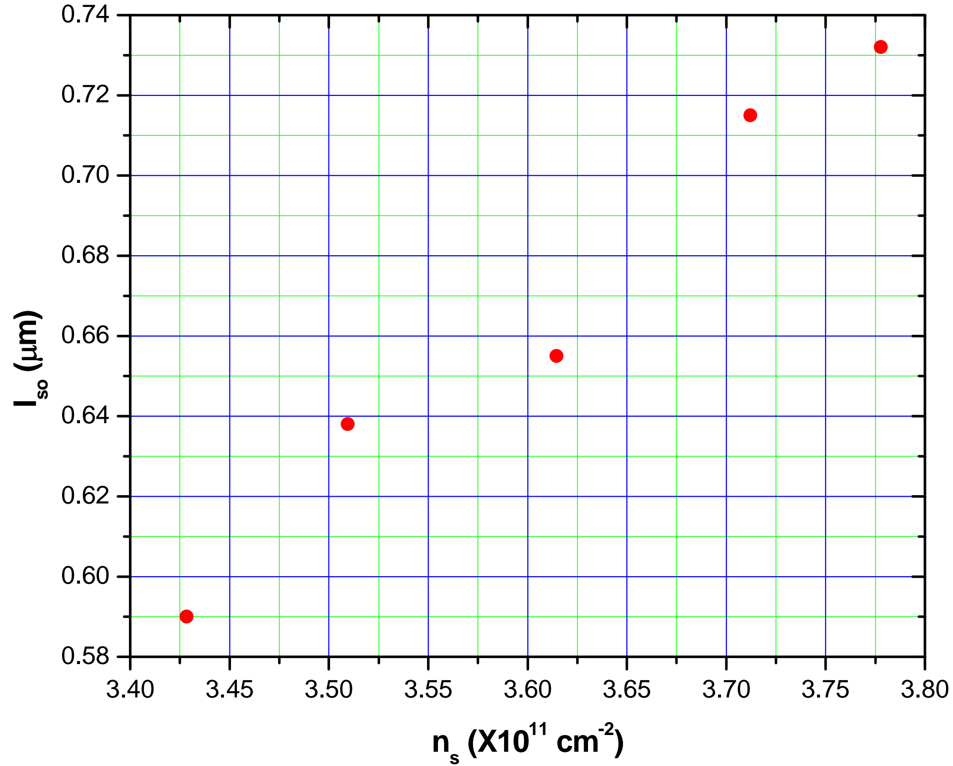

Figure 5.6 Dependence of spin-orbit length for HLN fittings on the electron density of the quantum well

The effective Rashba spin-orbit coupling constant α includes contributions from the built-in electric field across the quantum well as well as from the penetration of the electron wave function into the $Al_{x}In_{1-x}Sb$ barrier layers [6]. Experimentally extracted α values for different densities are shown in figure 5.7. A monotonic decrease in α with increasing carrier density was observed suggesting that the degree of structural inversion asymmetry decreases with an increase in density. For the limited gate voltage range we

have been able to change α from 3.29 X 10^{-12} eVm to 2.68 X 10^{-12} eVm which is a 23% change.

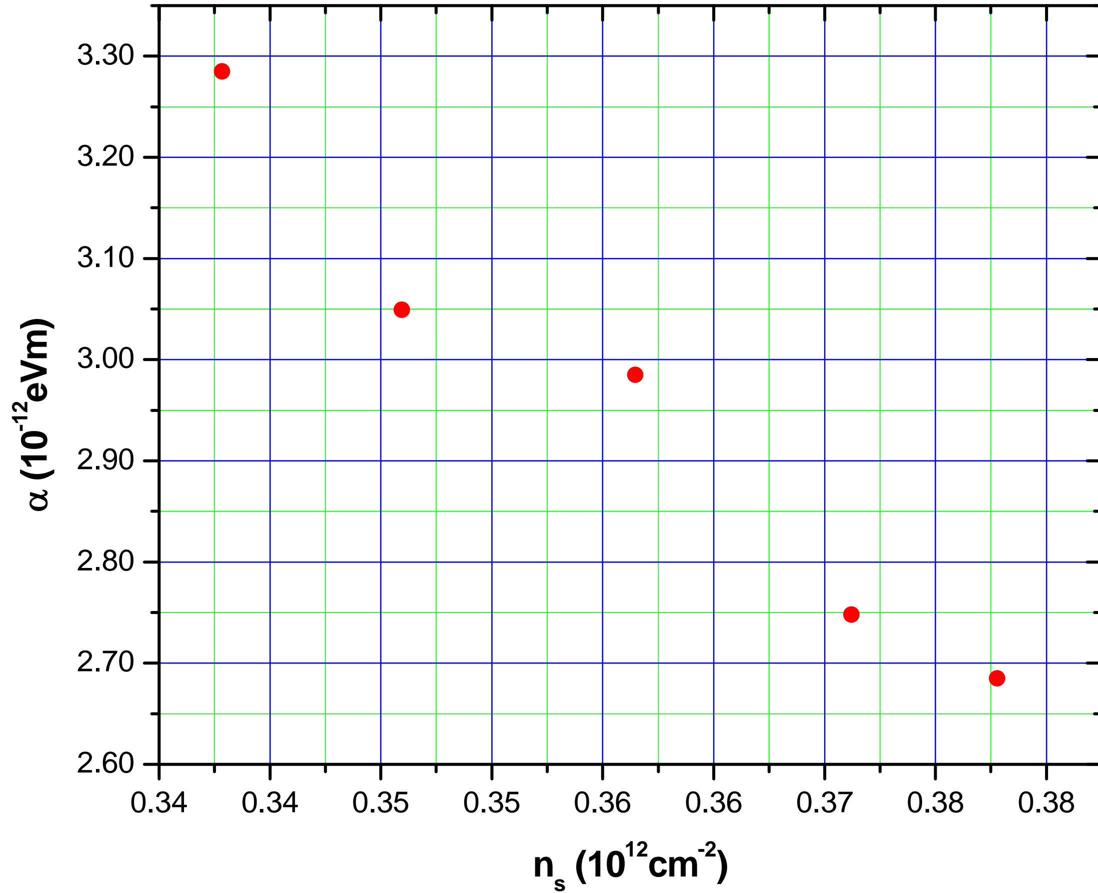

Figure 5.7 Behavior of α values extracted from HLN fittings on the carrier density

5.4 Weak antilocalization of symmetric samples

Samples from four different wafers were used to analyze spin-orbit effects of symmetrically-doped quantum well structures. Details of the sample structures including mobility and density at 4.2 K are listed in table 5.4.

Sample ID	Al%	Well Width (Å)	Carrier Density (n_s) at 4.2 K (cm^{-2})	Mobility (μ) at 4.2 K(cm^2/V.Sce)
S372	9	300	3.03×10^{11}	190000
S912	15	230	5.30×10^{11}	80000
S862	15	250	$3. 39 \times 10^{11}$	32000
S901	15	250	4.45×10^{11}	38000

Table 5.4 Sample parameters for symmetrically doped InSb/AlInSb heterostructures

For samples from wafers s372 and s912, HLN theory is not appropriate for the extraction of spin-orbit parameters because of the high mobility associated with them. Figures 5.8 and 5.9 clearly indicate the incompatibility of HLN theory for these traces.

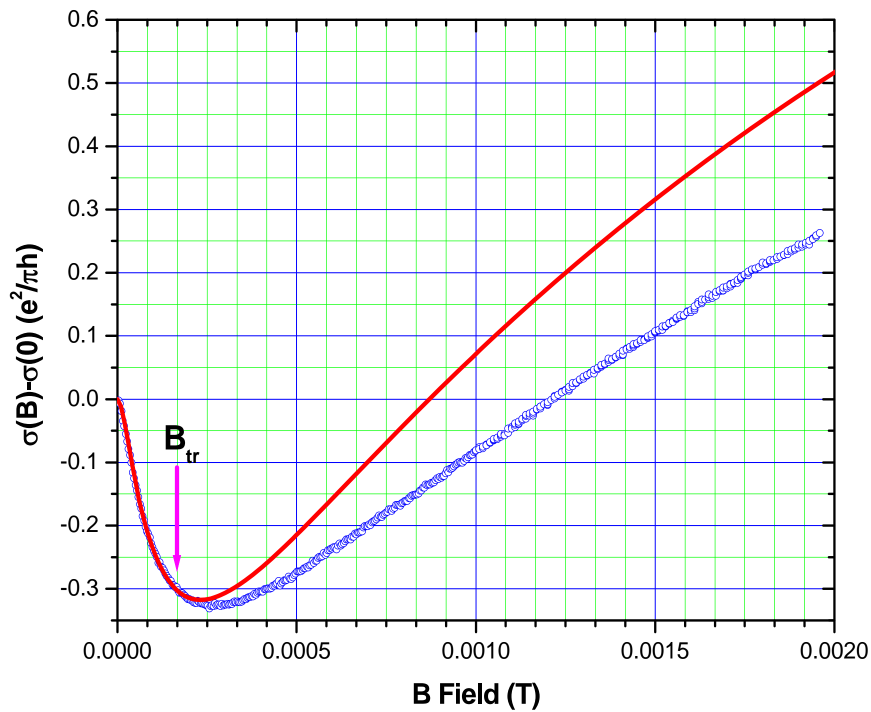

Figure 5.8 HLN fitting (solid curve) for s372 at 4.2K

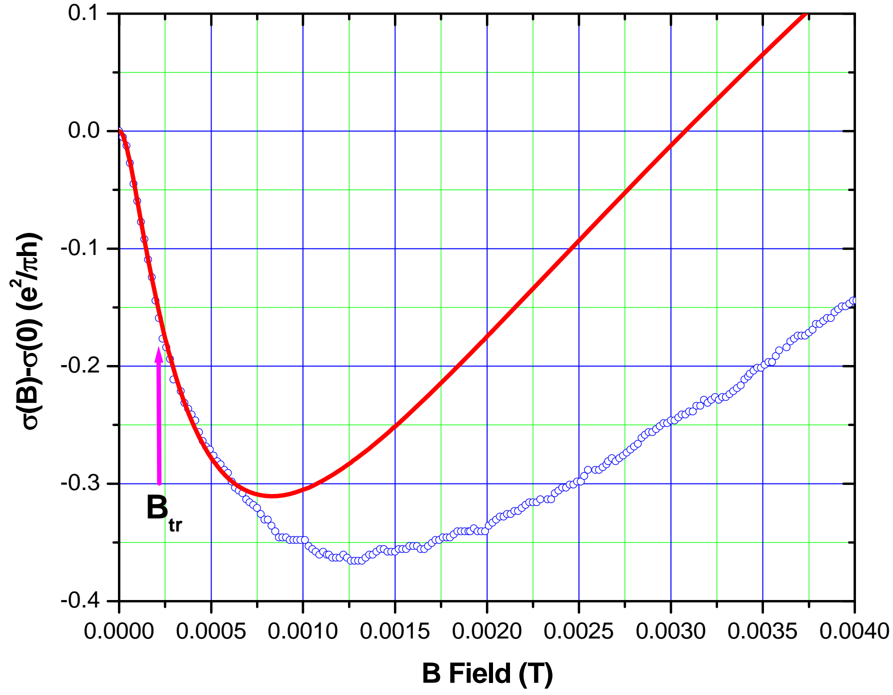

Figure 5.9 HLN fitting (solid curve) for s912 at 4.2

Therefore fittings for S372 and must be based on a theory beyond the diffusive regime [16], however weak antilocalization signals obtained from sample S862 and S901 were well fit by the HLN model as shown in figure 5.10.

For symmetrically doped samples, an estimate of Dresselhaus spin-orbit coupling constant can be calculated from characteristic magnetic field H_{so} obtained from the fitting routine for different ratios of relaxation times τ_1/τ_3 where τ_n is defined as

$$\frac{1}{\tau_n} = \int (1-\cos n\theta) W(\theta) d\theta \qquad 5.6$$

Here $W(\theta)$ is the probability that the electron wave vector changes direction by an angle θ per unit time due to elastic scattering [5]. One can obtain equation 2.2 in chapter 2 by assigning $n=1$ in equation 5.6.

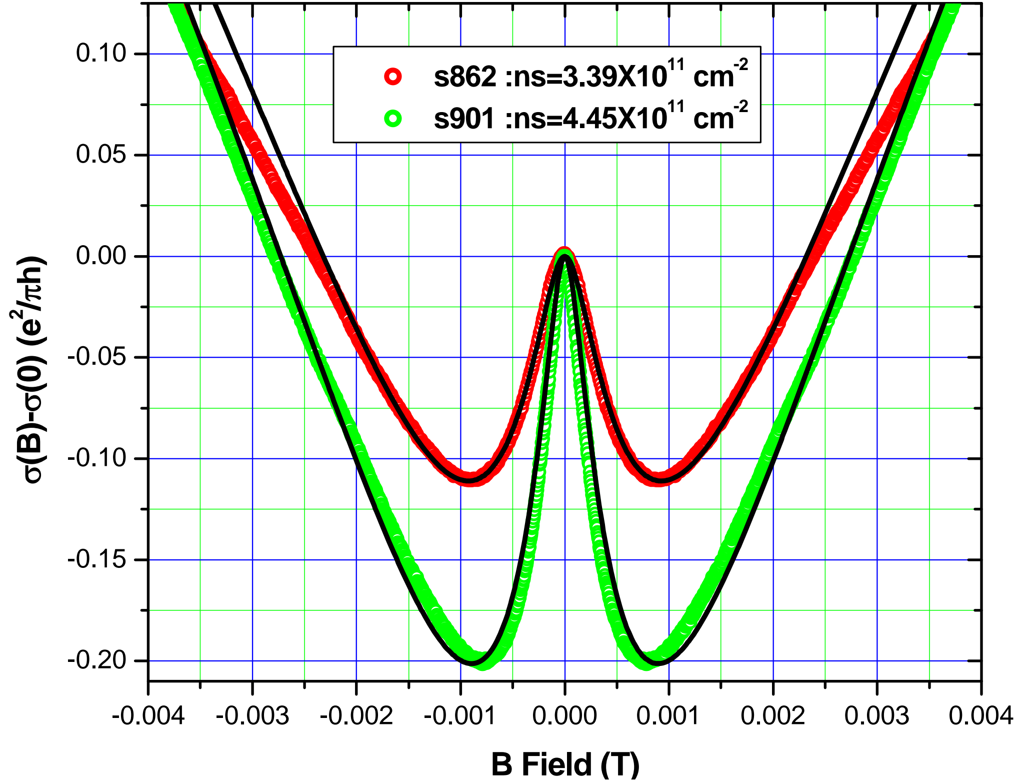

Figure 5.10 Conductivity corrections for s862 and s901 along with HLN fittings (black solid line)

The extracted Dresselhaus spin-orbit coupling constant for different τ_1/τ_3 ratios are shown in table 5.5. Despite the incompatibility of HLN fitting for samples s372 and s912, we include the fitting parameters to compare them with parameters from samples s862 and s901. The ratio τ_1/τ_3 was changed to examine the resulting change in the Dresselhaus spin-orbit coupling constant. By comparing it to the theoretically predicted value of $\gamma = 760\, eV\AA^3$ we can predict the type of scattering involved in the weak localization process [59].

Sample ID		$H_{\phi}\left(10^{-4}\,T\right)$	$H_{so}\left(10^{-4}\,T\right)$	τ_1/τ_3	$\gamma\ (eV\AA^3)$
Ballistic	S372	0.12	0.57	1	316
				2	447
				6	774
Ballistic	S912	0.44	1.94	1	327
				2	470
				6	815
Diffusive	S862	1.16	2.48	1	588
				2	832
Diffusive	S901	0.72	2.29	2	608
				3	745

Table 5.5 HLN fitting parameters along with extracted Dresselhaus spin-orbit constants for different τ_1/τ_3 ratios

Due to the existence of threading dislocations which run through the quantum well structure we expected to have large angle scattering (isotropic scattering) [5, 29]. For this type of scattering the probability $W\left(\theta\right)$ in equation 5.2 is independent of θ and the ratio of τ_1/τ_3 will be unity. In the case of small angle scattering, the ratio of τ_1/τ_3 is 9.

For samples S862 and S901, the γ values extracted are in the range of $745-832\,eV\AA^3$ for a τ_1/τ_3 ratio ranges from 2 to 3. This range of τ_1/τ_3 is quite acceptable for our samples and the predicted range for γ is in good agreement with the theoretical value of Dresselhaus spin-orbit coupling constant for InSb $(760\,eV\AA^3)$. The γ values extracted

from the fitting parameters obtained from samples s372 and s912 are in the range of $774-815\,eV\AA^3$ for values of the ratio of τ_1/τ_3 equal to 6 which is unphysical for our samples. This fact further verifies the inadequacy of HLN theory for these samples which are in the ballistic regime.

5.5 Conclusion

In conclusion, we have observed weak antilocalization in InSb/$Al_xIn_{1-x}Sb$ quantum well structures. The linear temperature dependence of the phase breaking rate indicates that the electron-electron interaction is the dominant inelastic scattering mechanism for phase relaxation from 1K to 10K. Although we have been able to achieve only a small change (10%) in carrier density from the back gating, the effective Rashba term changed by 23% indicating Rashba spin-orbit coupling is dominant for asymmetrically doped samples. This effective Rashba spin-orbit coupling constant contains the contributions from both the built-in electric field across the quantum well as well as the penetration of the electron wave function into the $Al_{.x}In_{1-x}Sb$ barrier layers. For samples in which isotropic scattering is dominant, the extracted Dresselhaus spin-orbit coupling constants are in good agreement with theoretically predicted results. For those systems in the ballistic regime, a theory beyond the diffusive limit is required. Fitting on data from these ballistic systems is a future effort that will require calculations with theorists.

Chapter 6

Spin polarized magnitotransport in InSb quantum well structures

6.1 Introduction

Transverse electron focusing in a two dimensional electron system (2DES) was first reported about twenty years ago by Van Houten *et al*. [60]. Since then there has been considerable interest in electron focusing in different heterostructures and geometries in the ballistic electron transport regime [61,62,63]. Fabrication of different geometries consisting of both quantum point contacts and quantum dots were made possible by the existence of a long mean free path $\left(l_e \sim 40\mu m\right)$ of these 2DES. In these devices both the injector and collector can be tuned to emit and accept spin polarized electrons using an in-plane magnetic field [61]. This paved the way to produce and detect spin polarized currents without using ferromagnetic materials which is one of the goals of spintronics. In this chapter we discuss transverse magnetic focusing in the ballistic regime under the influence of the Rashba and Dresselhaus spin-orbit interactions.

6.2 Basis of transverse magnetic focusing of electrons

The transverse magnetic focusing devices discussed in this thesis consist of two narrow constrictions separated by a distance *L* which is smaller than the mean free path of the 2DES. The schematic of a typical magnetic focusing device is shown in figure 6.1. The electron focusing originates from the classical cyclotron motion in a perpendicular magnetic field for electrons.

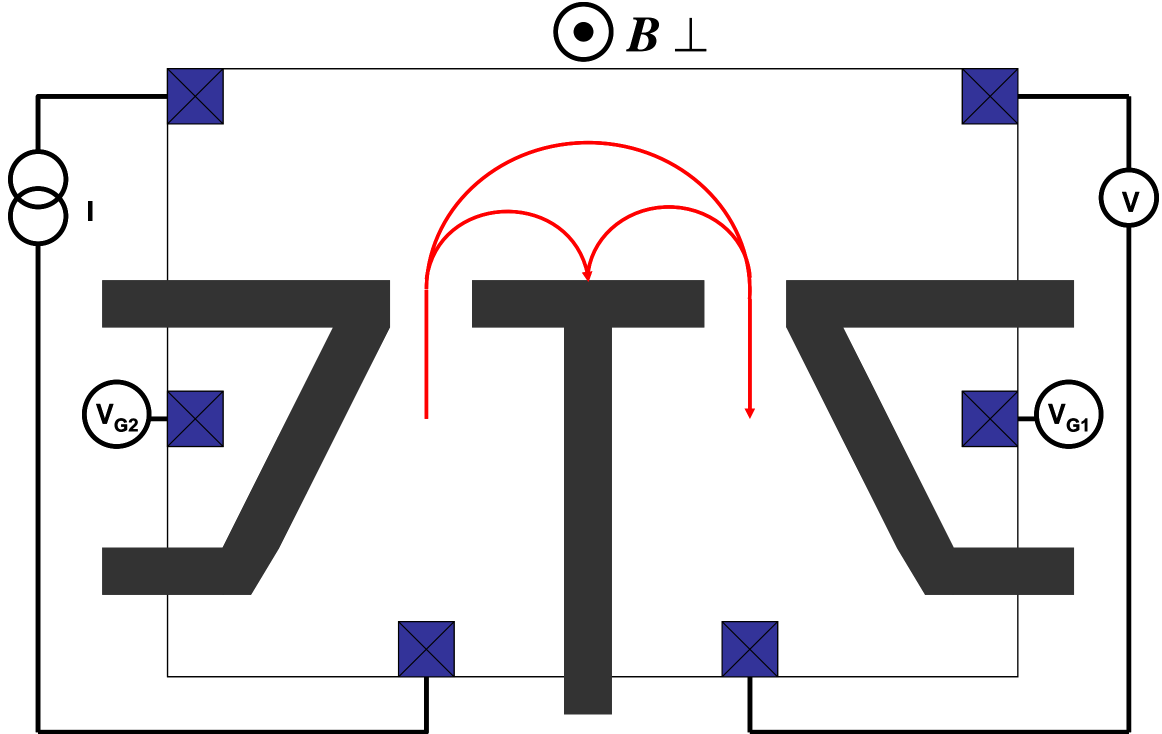

Figure 6.1 Schematic of the transverse electron focusing geometry, the black area represent trenches in the structure so that electrical contact is possible only through the constrictions

In the presence of a perpendicular magnetic field, electrons injected from the emitter can be detected by the collector after zero or more reflections from the boundary between them. The electron flux at the collector reaches a maximum whenever the constriction separation L is equal to an integer multiple of the cyclotron diameter $d_c = \frac{2\hbar k_f}{eB_\perp}$, hence there is a maximum in the collector voltage whenever the applied perpendicular magnetic field $B_\perp = pB_{\perp focus}$, $p = 1, 2, \ldots\ldots..$ where:

$$B_{\perp focus} = \frac{2\hbar k_f}{eL} \qquad 6.1$$

where k_f is the Fermi wave vector and e is the electron charge. For a constant injector current, the voltage on the collector is proportional to the incident electron flux. This implies equidistant peaks in the magnetoresistance traces, these peaks vanish if one reverses the direction of the perpendicular magnetic field into the non-focusing configuration by reversing the applied perpendicular magnetic field [60].

6.3 Spin splitting due to spin-orbit interactions

In systems possessing inversion symmetry, spin degeneracy exists due to the combination of spatial inversion symmetry $E(\vec{k},\uparrow)=E(-\vec{k},\uparrow)$ and time inversion asymmetry $E(\vec{k},\uparrow)=E(-\vec{k},\downarrow)$ which results in $E(\vec{k},\uparrow)=E(\vec{k},\downarrow)$, however in the absence of inversion symmetry, the spin degeneracy is lifted generating two energy surfaces for spin-parallel and spin-anti parallel to the effective magnetic field [59].

The energy dispersion due to bulk inversion asymmetry (BIA) for III-V 2DES in a quantum well grown in the $[001]$ crystallographic direction is given by;

$$E_{\pm}(k)=\frac{\hbar^2 k_{\parallel}^2}{2m^*}\pm\left[\left(\Omega_{D1}+\Omega_{D3}\right)^2-4\Omega_{D1}\Omega_{D3}\sin^2(2\phi)\right]^{\frac{1}{2}} \qquad 6.2$$

where $k_{\parallel}^2=k_x^2+k_y^2$ and $\tan\phi=k_y/k_x$. The terms Ω_{D1} and Ω_{D3} are the linear and cubic Dresselhaus terms, we adopt the same notations used in section 1.2 in equation 6.2. The spin-split energy surfaces have four-fold symmetry as shown in figure 6.2. Electrons moving in the x direction have spin polarization in x direction and the same for the y direction, however for $\phi=\frac{\pi}{4},\frac{3\pi}{4},\frac{5\pi}{4},\frac{7\pi}{4}$ the spin polarization is perpendicular to $\vec{k}_{\parallel}$,

therefore we cannot define a simple relationship between the quantization axis of the spins and wave vector $\vec{k}_{\parallel}$.

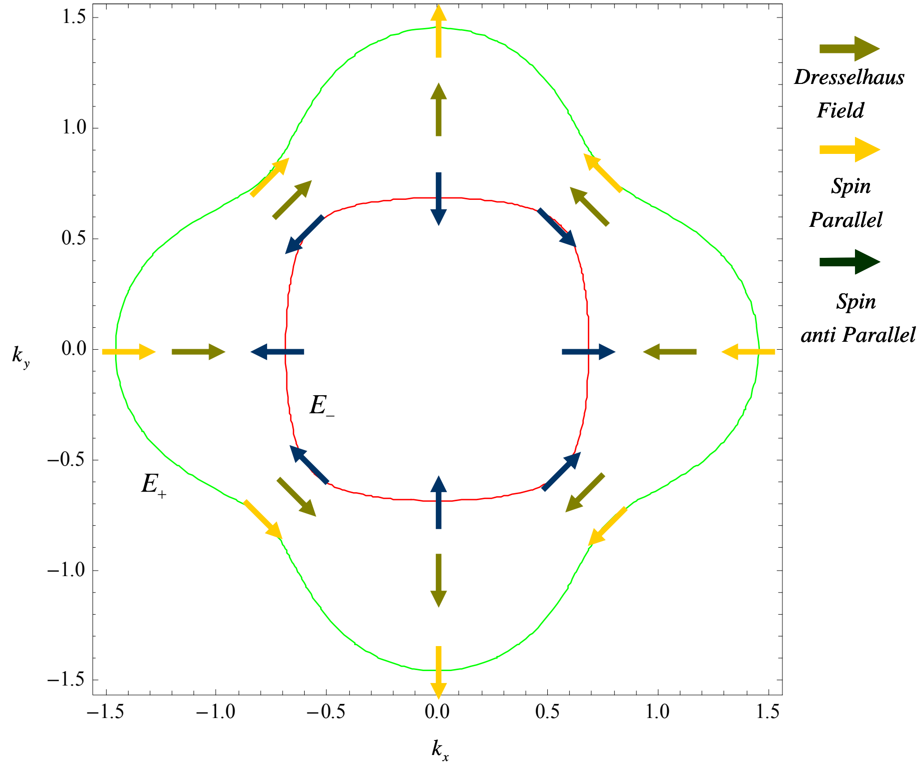

Figure 6.2 Fermi surfaces of spin sub bands due to the Dresselhaus spin-orbit interaction

In the case of the structural inversion asymmetry (SIA), the Rashba spin splitting is given by;

$$E_{\pm}(k) = \frac{\hbar^2 k_{\parallel}^2}{2m^*} \pm \Omega_{R1} \qquad 6.3$$

where Ω_{R1} is the Rashba spn-orbit energy. Since Ω_{R1} does not have a dependence on the polar angle ϕ, the splitting is isotropic in $k_{\parallel}$ Figure 6.3 shows the energy dispersion relation of the spin split bands along with the directions spins and effective Rashba magnetic fields.

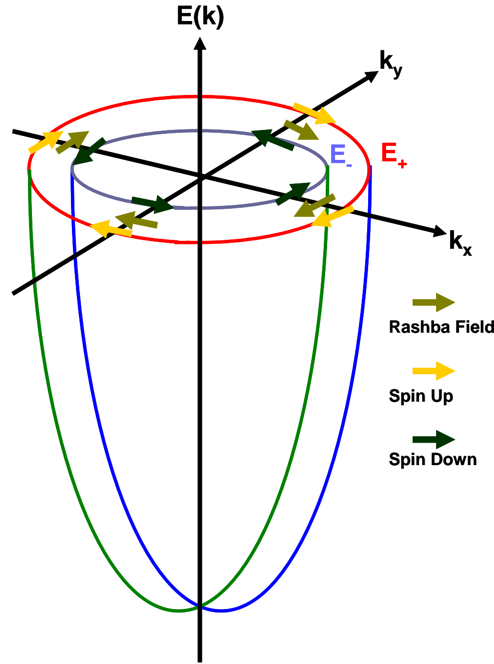

Figure 6.3 Energy dispersion relations for spin sub bands due to Rashba spin-orbit interaction

Unlike the Dresselhaus spin splitting, the spin quantization axis is always perpendicular to the wave vector $\vec{k}_{\|}$. If both the Rashba and Dresselhaus terms are present, the spin split energy contours become more complex, however for small $k_{\|}$ values, the $k_{\|}^3$ terms in Ω_{D1} and Ω_{D3} can be neglected, resulting Ω_{D1} is a term linear in $k_{\|}$ and $\Omega_{D3} \sim 0$. This paves the way to isotropic spin splitting which is independent of the direction of $k_{\|}$. In this limit, the combined effect has a simpler form for comparable Rashba and Dresselhaus strengths. Figure 6.4 (b) shows the two Fermi energy contours along with spin orientations for each of spin split bands for Dresselhaus spin splitting in small $k_{\|}$ limit. Figure 6.4 (c) illustrates the contribution from both terms with equal strengths. The interference between the two isotropic terms results in anisotropic energy contours [60].

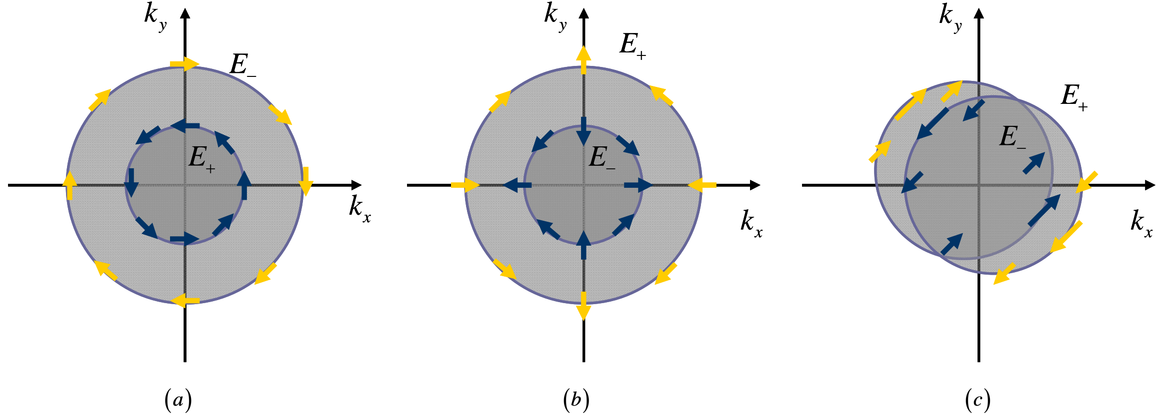

Figure 6.4 Fermi energy contours and spin quantization directions for spin-split bands. (a) Rashba spin-orbit interaction; (b) Dresselhaus spin-orbit interaction; (c) Equal amplitudes of Rashba and Dresselhaus terms

In the small $k_{\|}$ limit, the energy dispersion relation under the Rashba or Dresselhaus spin-orbit interaction for a 2DEG grown on $[001]$ direction can be written as;

$$E_{\pm}\left(k_{\|}\right)=\frac{\hbar^{2}k_{\|}^{2}}{2m^{*}}\pm\eta k_{\|} \qquad 6.4$$

For the case of the Rashba spin-orbit interaction $\eta=\alpha$ and for Dresselhaus spin-orbit interaction $\eta=\gamma\left\langle k_{z}^{2}\right\rangle$. Figure 6.5 illustrates the energy dispersion for electrons with and without spin orbit effects. Rotation of the curves about the energy axis generates the energy surface in two-dimensions.

For a given $k_{\|}$ value there exist two states corresponding to parallel and anti parallel spin quantization with respect to effective spin-orbit field. At zero temperature all the states in the spin-split bands are filled up to the Fermi energy and have different $k_{\|}$ values, k_{+}

and k_-. These two wave vectors can be related to the unperturbed wave vector k_f using a dimensionless parameter δ which characterized the differences in Fermi radii [64].

$$k_+ = (1+\delta)k_f \qquad k_- = (1-\delta)k_f \tag{6.5}$$

The dimensionless parameter δ can be related to effective spin-orbit splitting parameter η using the unperturbed Fermi energy ε_f and the wave vector k_f by equation 6.6.

$$\delta = \frac{\eta k_f}{2\varepsilon_f} \tag{6.6}$$

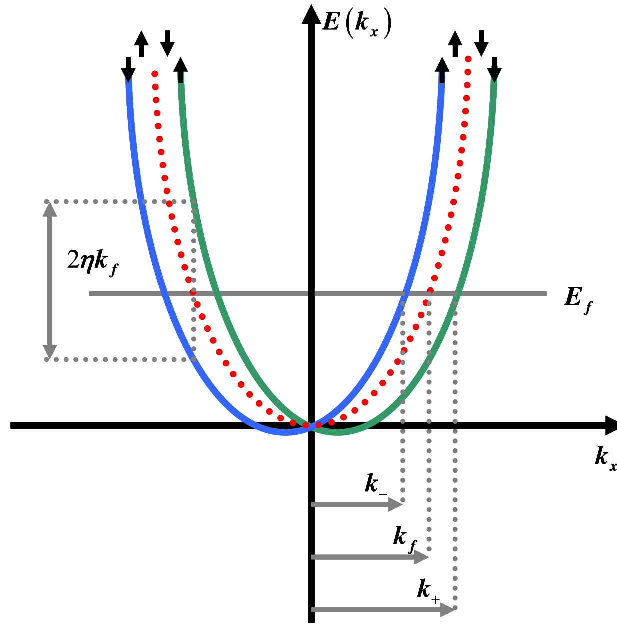

Figure 6.5 Energy dispersion relations for unperturbed bands (red dotted line) and spin spilt bands (green and blue solid lines)

The Fermi velocity the two spin sub bands is given by $v_f = \hbar^{-1}\left(\partial E/\partial k\right)_f$. Since the two energy contours have the same curvature, the Fermi velocities for the two bands are given by $v_f = \hbar k_f / m^*$.

6.4 Transformation of cyclotron orbits from momentum space to real space

Now that we have discovered that different spin projections in a system with strong spin-orbit interaction results different **k** values, it is necessary understand the transformation between k-space and real space orbitals.

In semi classical limit, the equation of motion of an electron wavepacket in momentum space (**k**-space) in an external magnetic field is given by;

$$\hbar \frac{d\boldsymbol{k}}{dt} = -e\boldsymbol{v} \times \boldsymbol{B} = -e\frac{d\boldsymbol{r}}{dt} \times \boldsymbol{B} \qquad 6.7$$

From equation 6.7, it is evident that the motion of real space is closely related to that of momentum space. The projection of the real space motion onto a plane perpendicular to the external magnetic field is same momentum space trajectory with a 90 degree rotation and scaled by a factor $\hbar/eB$.

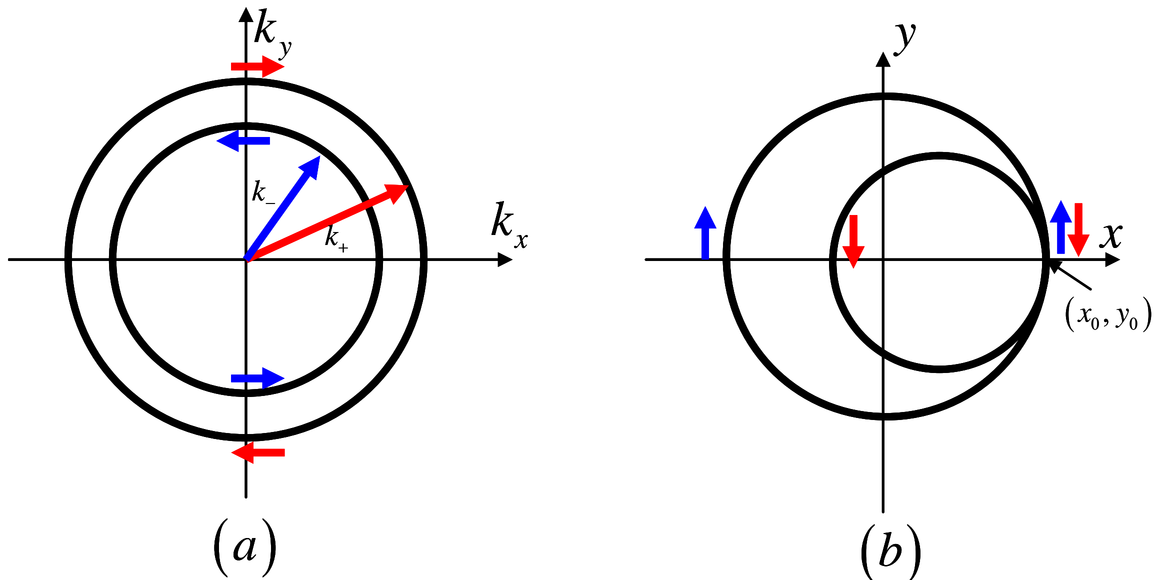

Figure 6.6 (a) spin-split energy contours due to spin-orbit interaction linear in momentum; (b) Projection of k- space orbits onto real space

In magnetic focusing experiments the real space spin dependent orbits have to emit at the same location $\left(x_0, y_0\right)$ into the injector constriction opening at $t = 0$, additionally only those electrons with $k = k_y, k_x = 0$ will pass through the constriction. Figure 6.6 shows the effect of these boundary conditions to the spin dependant trajectories in real space. For $t > 0$ these trajectories evolved along their respective Fermi surfaces giving different spin-splitting at different polar angles.

6.5 Spin polarized current focusing of InSb heterostructures

Due to the existence of a strong spin-orbit interaction in Insb/$Al_xIn_{1-x}Sb$ heterostructures, charge carriers at the Fermi energy have different wave vectors $k_{+,}$ k_- for spin parallel and anti-parallel to the effective spin-orbit field. Therefore in accordance with equation 6.1 in the presence of a weak perpendicular magnetic field, spin polarized charge carriers injected from a QPC will have different cyclotron diameters [65],

$$d_c^{\pm} = \frac{2\hbar k^{\pm}}{eB_{\perp focus}^{\pm}} \tag{6.8}$$

These two trajectories can be selectively focused into the detector with the appropriate perpendicular field. Figure 6.7 shows SEM micrographs of magnetic focusing device FOC-23 which has a lithographically set constriction width $w = 0.4\mu m$ and constriction separation $l = 0.3\mu m$.

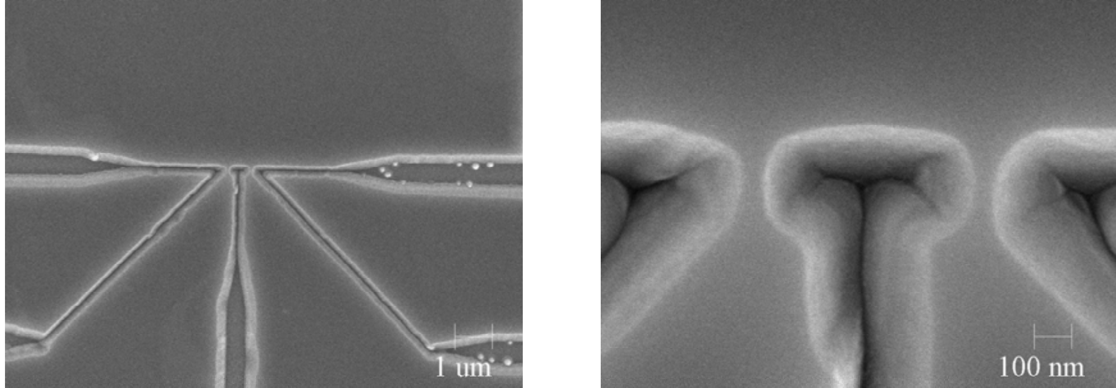

Figure 6.7 SEM micrographs for a typical electron focusing device FOC-23

The electron focusing measurements were made in a ^{3}He cryostat for temperatures ranging from 4.2K to 10K. Four terminal measurements were made by passing through a 100 nA peak to peak AC current through the injector while measuring the voltage across the detector as a function of perpendicular magnetic field. The magnetoresistance traces were then generated by dividing the voltage across the detector by the applied AC current and plotting them against the perpendicular magnetic field. Figure 6.8 shows typical magnetoresistance traces obtained from the magnetic focusing device FOC-41.

For this particular device, the constriction openings were lithographically set to $w = 0.3\mu m$ with separation $l = 0.3\mu m$ from each other implying a center to center separation of $L = 0.6\mu m$. A closer look at the magnetoresistance data inside the encircled region on figure 6.8 reveals that peaks appear at multiples of $B_{\perp focus} = 0.32T$ which is consistent with expected value for a carrier density of 3.3x10^{11} cm^{-2} and center to center separation of 0.6μm. As shown in figure 6.9 the first focusing peak is a doublet while the second focusing peak does not contain multiple peaks.

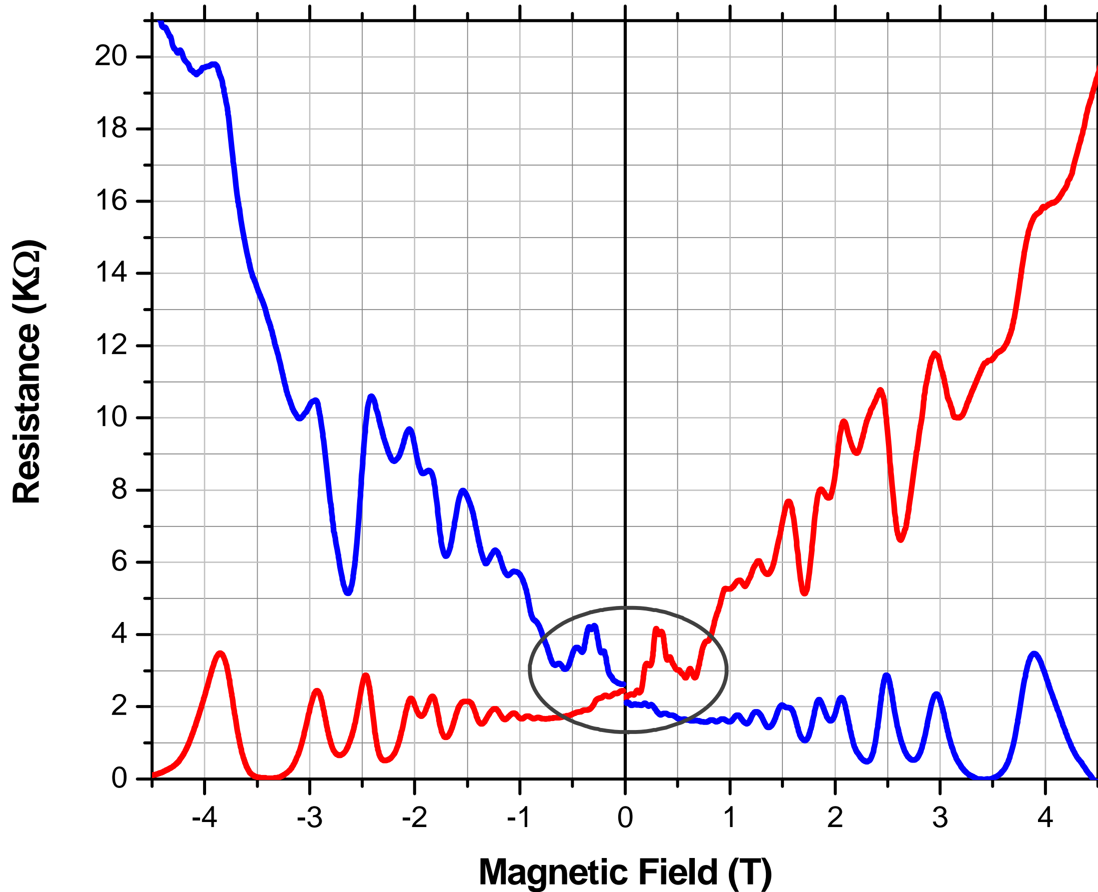

Figure 6.8 Transverse magnetic focusing data for Insb/$Al_xIn_{1-x}Sb$ heterostructures at 4.2K for device FOC41. In red trace focusing peaks appear in forward magnetic field direction. The blue trace was obtained by exchanging the injector and collector hence equivalent to magnetic focusing in reverse magnetic field direction

The higher order peaks are hard to distinguish because they superimposed with the characteristic Shubnikov-de Hass oscillations of the 2DES. We believe the doublet structure is due the existence of two different Fermi wave vectors at the Fermi energy as mentioned in section 6.2. The single second focusing peak is due the spin dependent

focusing trajectories after the reflection from the boundary has been predicted to average out the special separation between different spins.

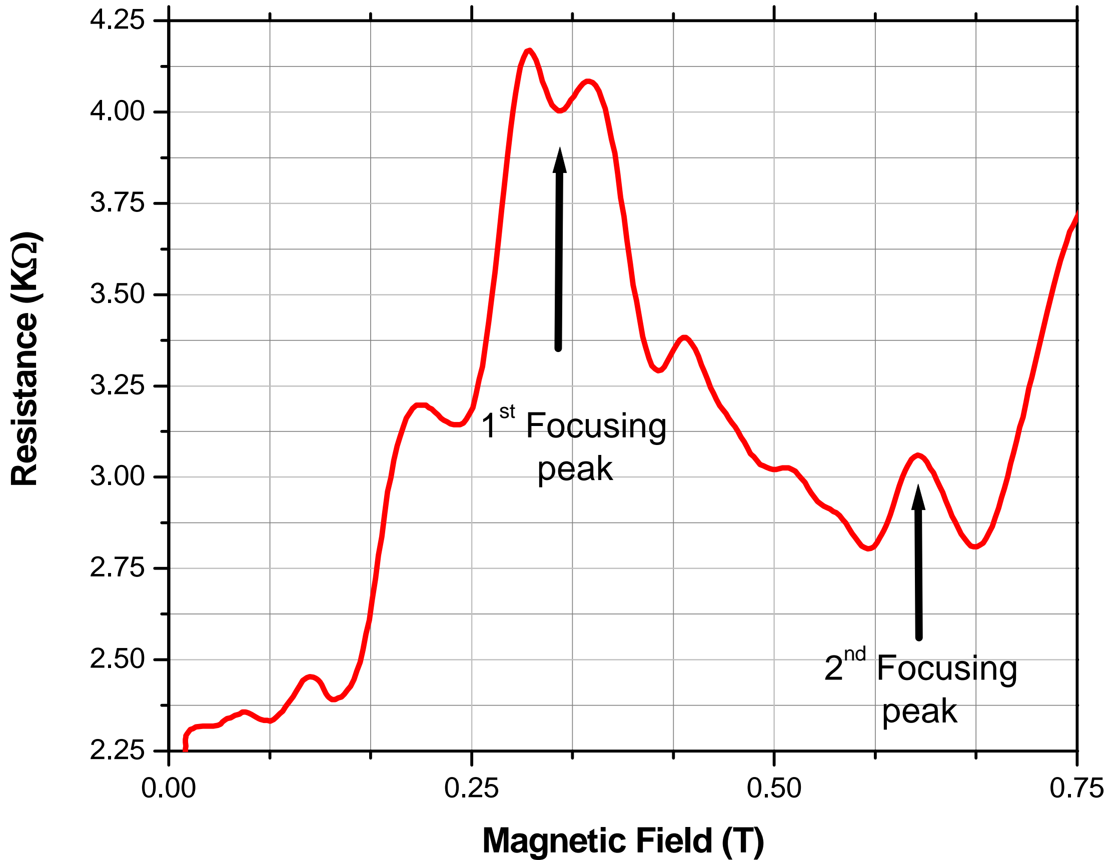

Figure 6.9 Nature of 1st and 2nd transverse magnetic focusing peaks for InSb/$Al_xIn_{1-x}Sb$ heterostructures at 4.2K

To isolate focusing peaks from universal conductance fluctuations, transverse magnetic focusing was performed at temperatures as high as 10K. The temperature independent and robust nature of peaks as shown in figure 6.10 confirms that the peaks are not due to universal conductance fluctuations.

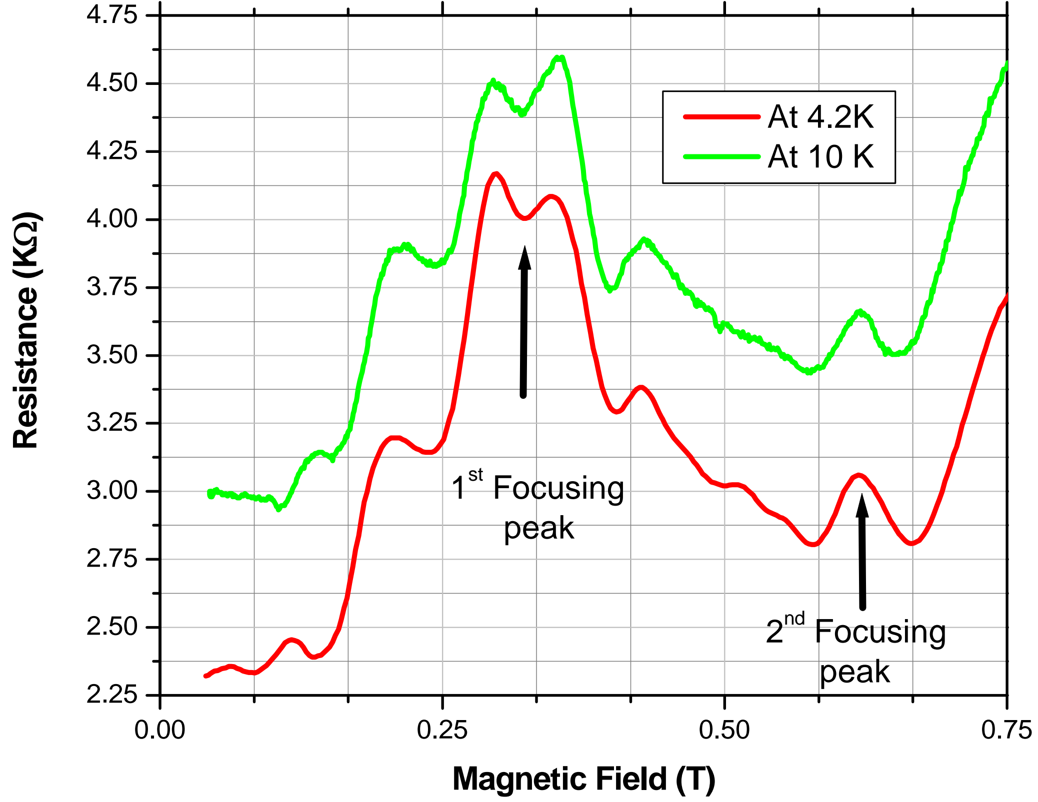

Figure 6.10Temperature evolution of transverse magnetic focusing peaks for InSb/Al$_x$In$_{1-x}$Sb heterostructures

This device was fabricated from wafer S941 which is a symmetrically doped sample and hence we expect only the Dresselhaus spin-orbit interaction. The effective spin splitting parameter $\eta = \gamma \left\langle k_z^2 \right\rangle$ can be calculated from the peak splitting using the equation 6.9.

$$\eta = \frac{\hbar e L}{4m^*}\left(B^+_{\perp focus} - B^-_{\perp focus}\right) \qquad 6.9$$

Using $B^+_{\perp focus} = 0.35 Tesla$, $B^-_{\perp focus} = 0.3 Tesla$ and $L = 0.6 \mu m$, the extracted Dresselhaus spin-orbit coupling constant $\gamma = 5400\, eV\mathring{A}^3$, which is a factor of 7 larger than the theoretically predicted value [59]. This calculation was done by neglecting the cubic

Dressulhaus term and assuming cyclotron effective mass is same as electron effective mass. These assumptions may have attributed to the discrepancy of extracted γ value.

6.6 Gate voltage dependence of current focusing peaks

The trenches used to define constrictions also define in-plane gates to control constriction widths as shown in figure 6.1.

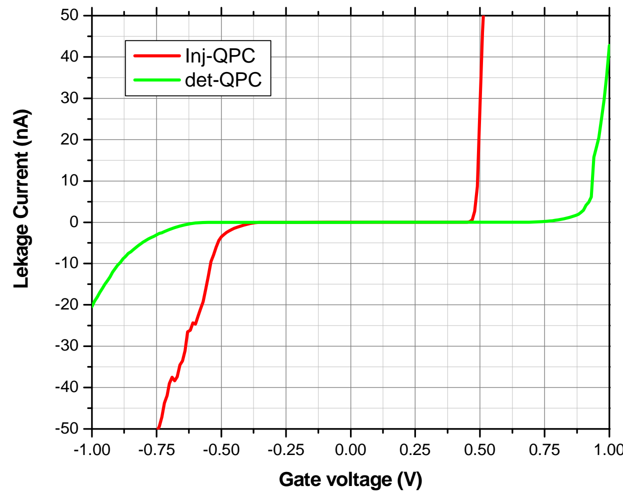

Figure 6.11 Gate leakage measurements for the constrictions for a typical current focusing device

The in plane gates have fairly good voltage ranges as shown in figure 6.11. The injector gate has voltage range of -0.40 volts to +0.50 volts and for the detector it was -0.6 volts to +0.75 volts (leakage current, $I < 0.25\ nA$).

Since the application of negative gate voltages to the constrictions only reduces the number of channels passing thought them, the focusing peaks must be independent of either injector or detector biasing. Figure 6.12 clearly indicates the robust nature of focusing peaks for different detector voltages for zero biased injector.

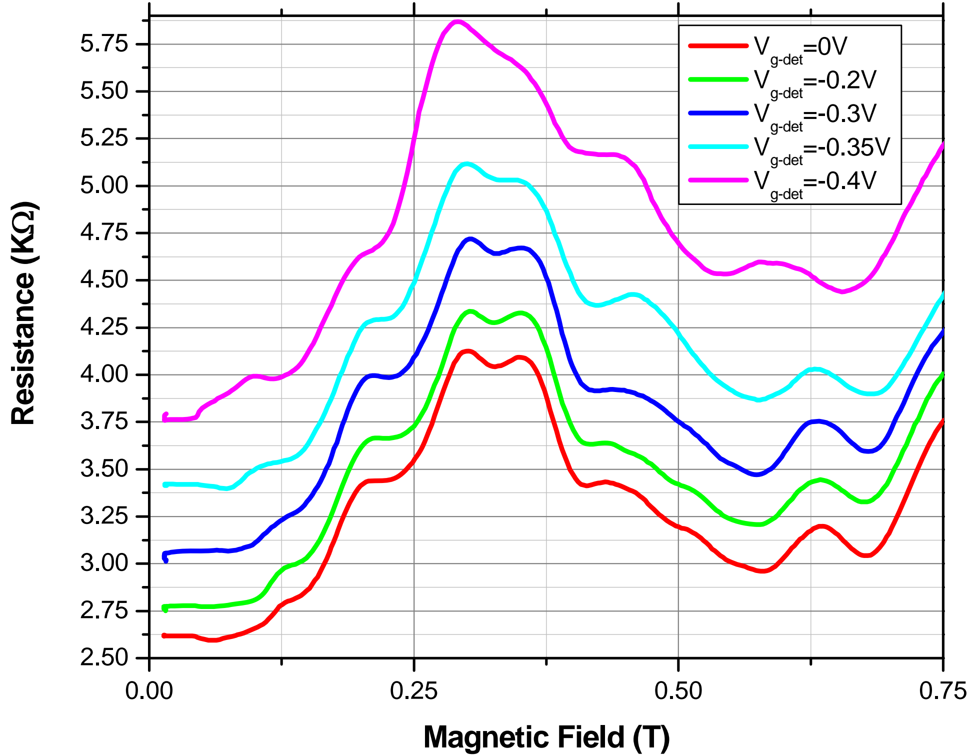

Figure 6.12 Robust nature of focusing peaks for different detector gate voltages. Traces have been shifter for clarity

6.7. Spin filtering of current focusing devices

In order to determine if the doublet is due to spin, we applied a parallel magnetic field to the sample to modify the energy contours by adding Zeeman energy.

In our experimental setup we only have a single superconducting coil to generate the magnetic field, hence had to tilt the sample in order to apply an in-plane magnetic fields while also providing the proper perpendicular magnetic field for electron focusing. The orientation of the magnetic fields with respect to the sample is shown in figure 6.13, the perpendicular and parallel magnetic field can be calculated by knowing the angle θ.

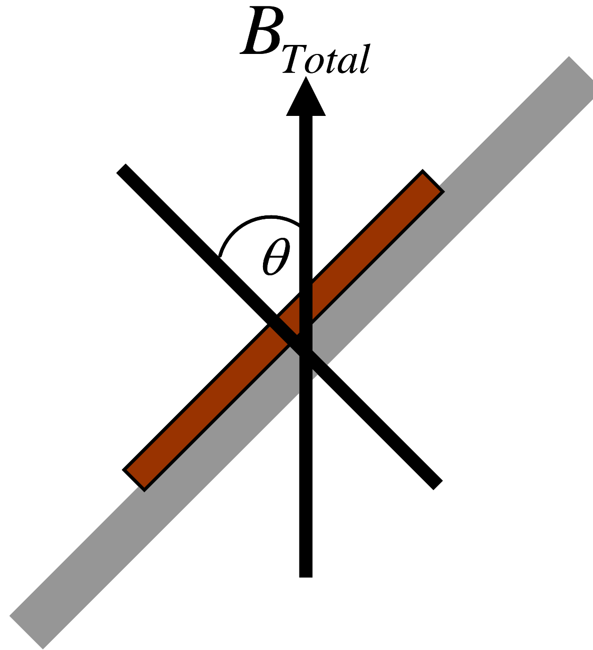

Figure 6.13 Schematic of the sample tilter setup for fixed magnetic field

The sample was mounted in a pivoting sample holder coupled by a Kevlar string to the linear displacement unit with Be-Cu spring providing restoring force. More detail about tilter assembly and calibration can be found in reference [67].

Regardless of the tilt angle the first magnetic focusing peak occurs at same. But the doublet nature of the first focusing peak evolves to a single peak at tilt angle of 80 degrees as shown in figure 6.14. At this angle in- plane magnetic field corresponding to $B_{\perp focus} = 0.31$ Tesla, was 1.56 Tesla. The Zeeman energy at $B_{\parallel} = 1.56\, Tesla$ was 2.3 meV. We believe the evolution of the doublet structure to a singlet is due to the modification of energy surfaces by the Zeeman energy.

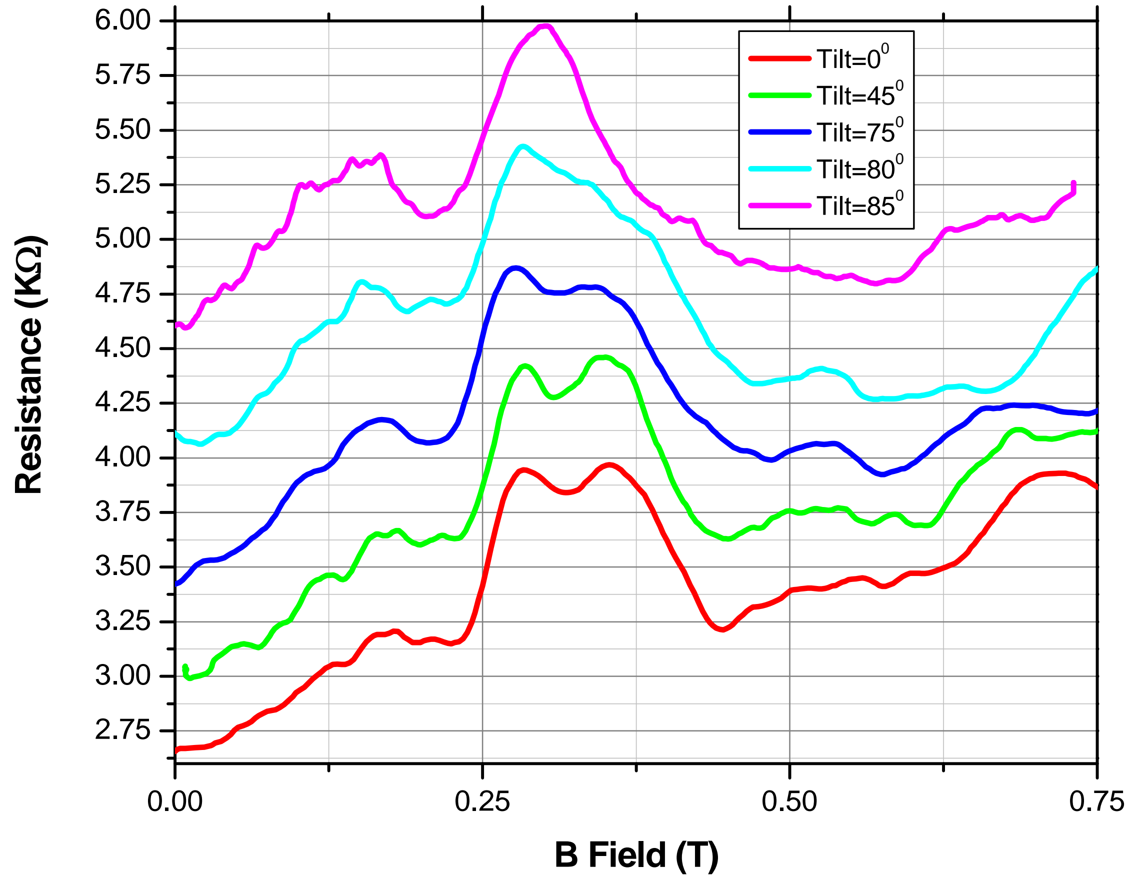

Figure 6.14 Evolution of the 1st focusing peak with different in-plane magnetic fields.

6.8 Current focusing of asymmetrically doped samples

Structures similar to the SEM micrographs in figure 6.7 were also fabricated for asymmetrically doped quantum wells from wafer S912 with a carrier density of 5.14x10^{11} cm^{-2}. Figure 6.15 indicates the magnetoresistance traces obtained for a device which has constriction openings $w = 0.3\mu m$ and edge to edge separation $l = 0.3\mu m$ from one another implying a center to center separation $L = 0.6\mu m$.

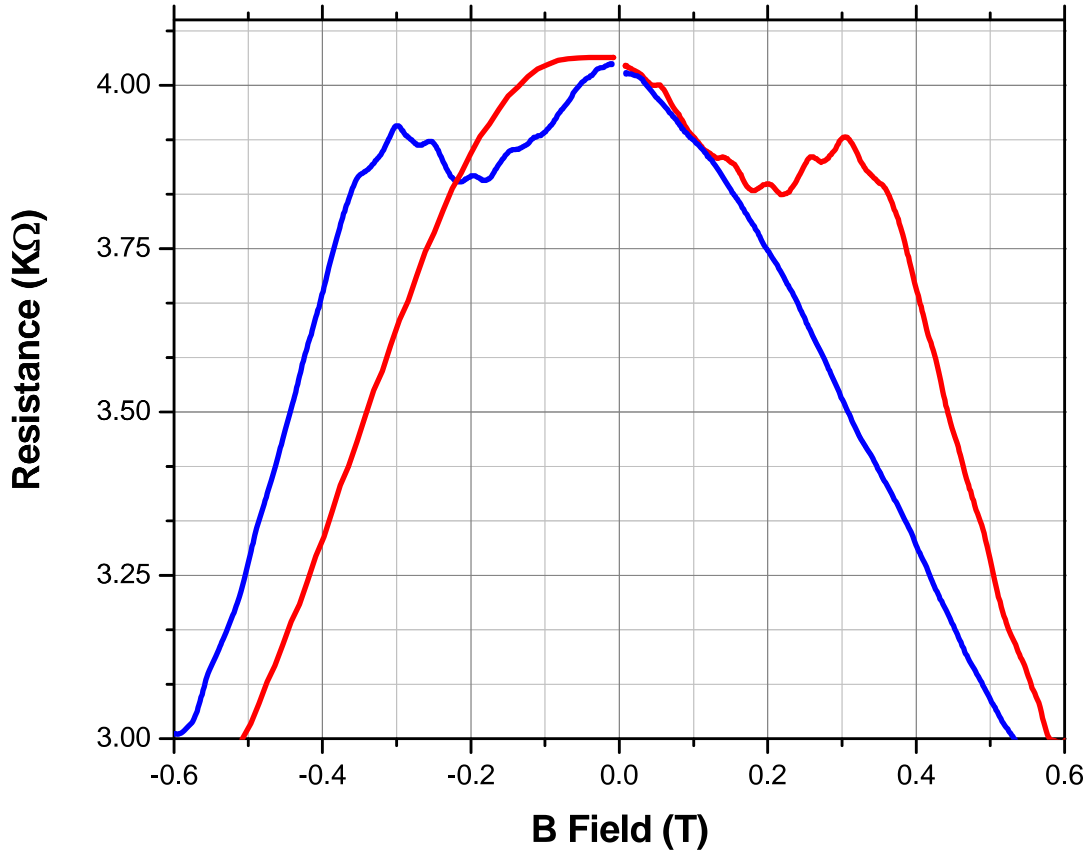

Figure 6.15 Transverse magnetic focusing data for asymmetrically doped Insb/$Al_xIn_{1-x}Sb$ heterostructures (FOC-76) at 4.2K. In red trace focusing peaks appear in forward magnetic field direction. The blue trace is obtained by exchanging the injector and collector

With calculated value of $B_{\perp focus} = 0.27\,Tesla$ for this device, similar the symmetrically doped structure discussed in section 6.5, a closer look at the magnetoresistance data reveals a doublet first focusing peak around, $B_{\perp focus} = 0.27\,Tesla$ see figure 6.16. However the second focusing peak was not detected on this device. Unlike the previous case we used $CH_4/H_2/Ar$ based RIE recipe to fabricate this device which has a tendency to create rough surface morphologies due to deposition of non volatile hydrocarbon

compounds. The absence of the second focusing peak could be attributed to surface roughness of reflection plane.

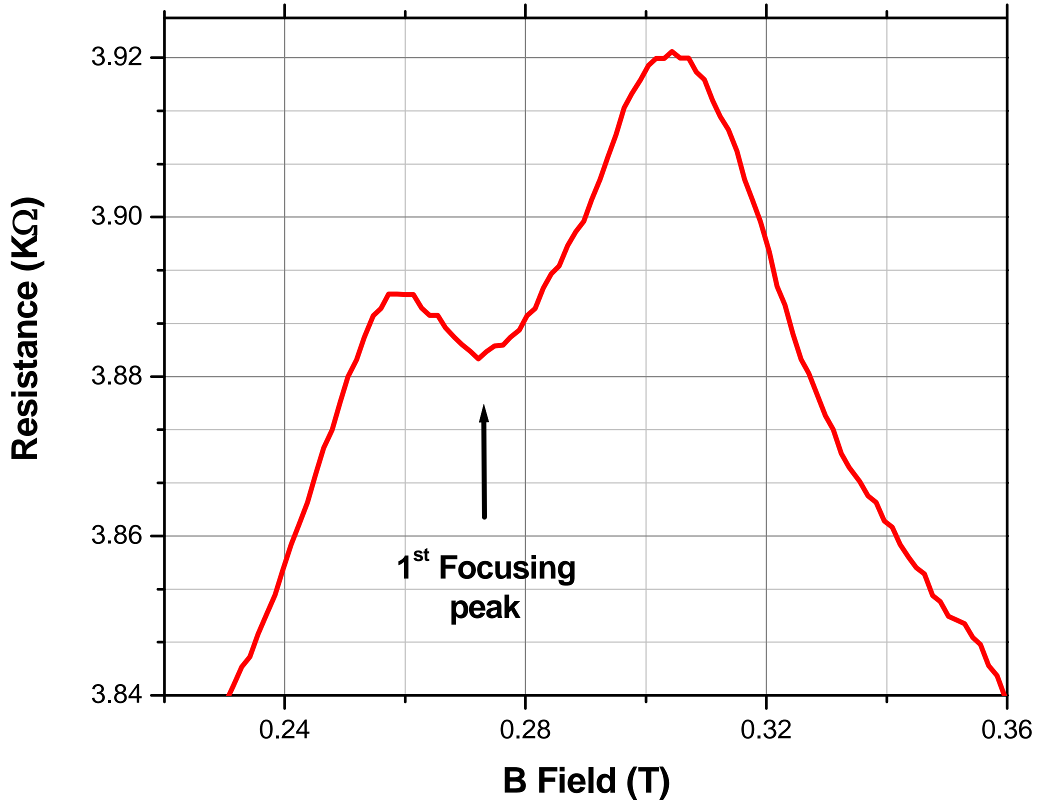

Figure 6.16 Doublet structure of 1st transverse magnetic focusing peak for asymmetrically doped InSb/AlxIn1-xSb heterostructure

Using $B^{+}_{\perp focus} = 0.30 Tesla$, $B^{-}_{\perp focus} = 0.26 Tesla$ and $L = 0.6 \mu m$, the extracted Rashba spin-orbit coupling constant $\alpha = 1.98 \times 10^{-11}\ eVm$, during this calculation we neglect the contribution from the Dresselhaus contribution.

Asymmetrically doped $InSb/Al_xIn_{1-x}Sb$ heterostructures have both Dresselhaus and Rashba spin-orbit interactions and the combination of these two contributions result in different Fermi contours depending on their relative strengths. The nature of the spin-split

Fermi contours under the influence of comparable amounts of Dresselhaus and Rashba spin-orbit coupling are shown in figure 6.17.

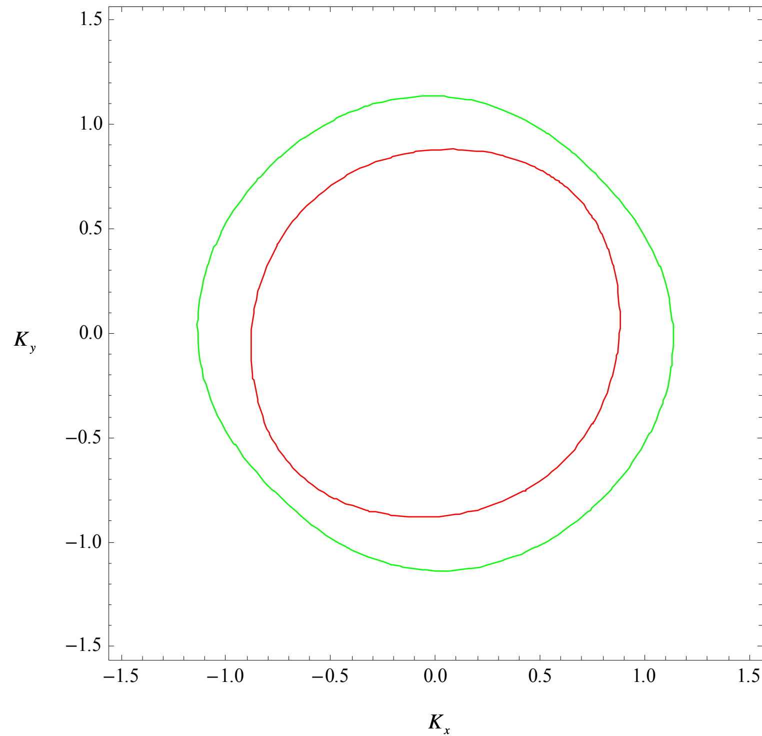

Figure 6.17 Fermi contours of spin-split bands under the influence of Dresselhaus and Rashba spin orbit interaction

As mentioned in section 6.5, different amounts of spin separation at the detector end can be achieved by orienting the injector and detector constrictions with an angular separation of 90 and 135 degrees between them. Based on this, current focusing devices were fabricated to achieve different spin separation at the detector. Both 90 and 135 degree geometries were fabricated using wafers T134 and T145. Figure 6.18 show SEM micrographs of focusing devices fabricated using BCl_3/Ar RIE on wafer T145.

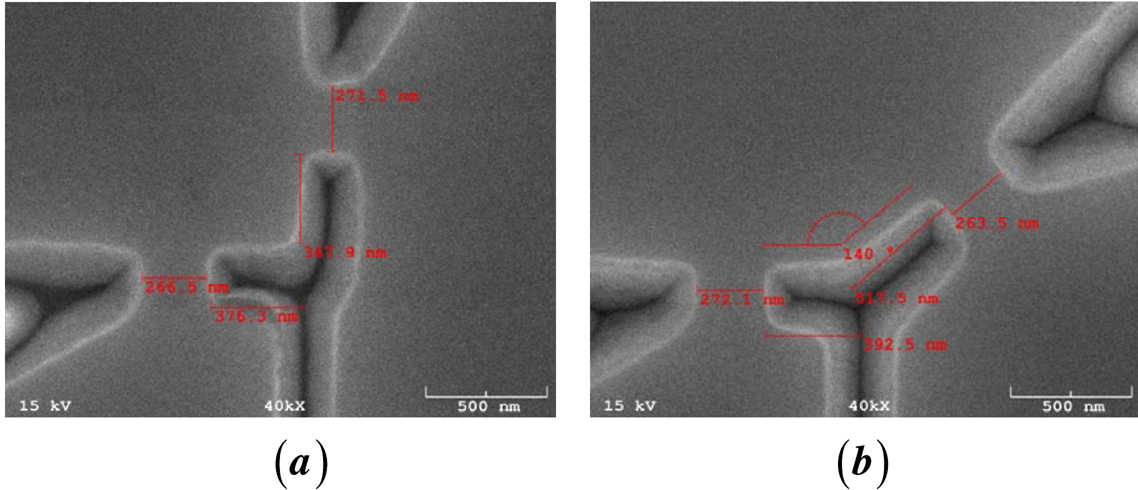

Figure 6.18 SEM micrographs of (a) 90 degree (FOC-107); (b) 135 degree (FOC111) electron focusing device

The magnetoresistance traces obtained for two 90 degree devices FOC 99 and FOC 100 are shown in figure 6.19. The first device has constriction opening of $w = 0.3\mu m$ and $l = 0.3\mu m$ from the center of the reflection surface to the edge of constriction, for the second device $w = 0.4\mu m$ and $l = 0.3\mu m$. For these two devices, we expect to have focusing magnetic field values of 0.26 Tesla and 0.24 Tesla respectively.

On both devices there was no clear indication of focusing peaks at the expected perpendicular magnetic fields; however there were some prominent peaks present on the magnetoresistant traces, whereas for the non focusing configuration, no such peaks detected. We observed similar behavior on 135 degree focusing devices fabricated on wafer T134.

We believe these peaks are related to combination of quantum interference and electron magnetic focusing. Further experiments have to be carried out in order to verify the

isolate magnetic focusing peaks in the magnetoresistance traces such as internal magnetic focusing of array of ballistic cavities [68].

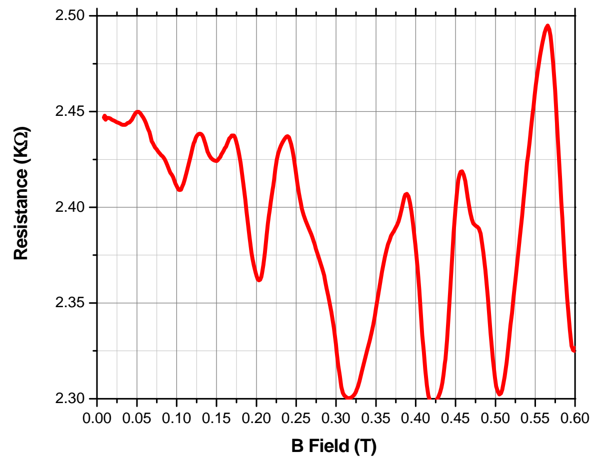

(a)

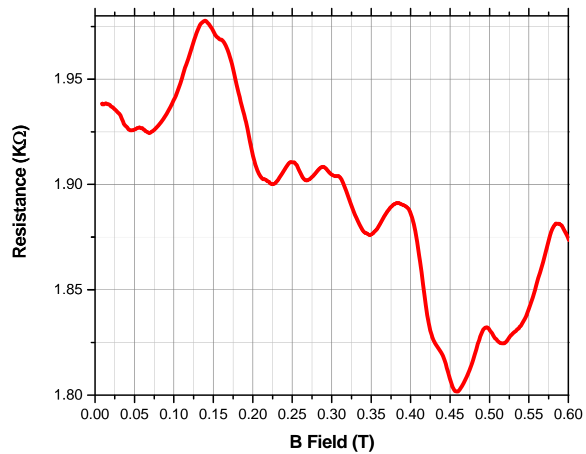

(b)

Figure 6.19 Transverse magnetic focusing data for asymmetrically doped 90 degree focusing device (a) $w = 0.3\ \mu m; l = 0.3\ \mu m$ (FOC 99): (b) $w = 0.4\ \mu m; l = 0.3\ \mu m$ at 4.2K (FOC 100)

6.9 Conclusion

Electron magnetic focusing was observed for both symmetrically and asymmetrically doped InSb/$Al_xIn_{1-x}Sb$ heterostructures. The doublet structure present on the first focusing peak is a clear indication of strong spin-orbit interaction persists in these systems. The ability of magnetic focusing devices to function as spin filters has been demonstrated, this property is quite useful in the area of spintronics since these devices can generate non equilibrium spin population without ferromagnetic contacts. In the systems which have comparable amounts of Rashba and Dresselhaus spin-orbit interactions the interference between the two results in anisotropy of the spin splitting.

We have not been able to observe magnetic focusing on both 90 and 135 degree current focusing devices, to filter out focusing peaks from quantum interference peaks further experiments has to be conducted using multiple parallel magnetic focusing devices to smear out the interference effects.

Chapter 7

Conclusions and future work

7.1 Introduction

Implementation of successful semiconductor spintronic device involves efficient spin injection to the active region of the device, manipulation of spin orientations in the active region and successful detection at the detector end. In semiconductors, the manipulation of spin can be achieved in terms of spin-orbit interaction. Datta and Das have proposed spin field effect transistor (SFET) [69] which control the spin precession in the active region by applying different voltages. It is important to understand the strength of spin-orbit coupling in order to make functional spintronic devices from semiconductors. This thesis reports observation of weak antilocalization on InSb/$Al_xIn_{1-x}Sb$ for the first time and present estimations of the strength of spin-orbit coupling which arises from different asymmetries.

7.2 Conclusions

We have experimentally observed weak antilocalization in both diffusive and ballistic regimes. Theoretical data modeling performed for diffusive samples based on HLN theory and successfully obtained both Rashba and Dressulhaus spin orbit coupling parameters. Although we had a limited range of varying the density of electrons in 2DEG, for 10% change in density we observed a 23% change in Rashba coefficient which makes InSb a promising candidate for spintronic applications. There is about 20% difference between extracted and theoretical Dressuhaus constant.

We observed spatial separation of spin dependent trajectories from transverse magnetic focusing devices. The calculated spin-orbit parameters are very large compared to the values we extracted from weak antilocalization measurements.

7.3 Further work

In this thesis we only performed the data fitting for weak antilocalization in diffusive regime. We are in collaboration with Prof. L. E. Golub for the data modeling in ballistic regimes. The lack of credible top gating greatly hinders our experiments in tuning the Rashba spin-orbit parameter. A strong effort must be made to make top gates for $InS/Al_xIn_{1-x}Sb$ quantum wells.

In order to filter out focusing peaks in transverse magnetic focusing experiments we need to implement new device geometries consisting with multiple focusing structures in order to average quantum interference effects.

BIBLIOGRAPHY

[1] Joachim Kessler, *Polarized Electronics*, Springer-Verlag, Berlin Heidelberg New York (1976).

[2] Leonard I. Schiff, *Quantum Mechanics*, McGRAW-HILL Book Company.

[3] John David Jackson, *Classical Electrodynamics Third Edition.*

[4] Dresselhaus G. Phys. Rev. 100, 580 (1955).

[5] W. Knap, C. Skierbiszewski, A. Zduniak, E. Litwin-Staszewska, D. Bertho, F. Kobbi, and J. L. Robert, G. E. Pikus, F. G. Pikus, S. V. Iordanskii, V. Mosser, K. Zekentes, Yu. B. Lyanda-Geller, Phys. Rev. B 53, 3912 (1996).

[6] Th. Schäpers, G. Engels, J. Lange, Th. Klocke, M. Hollfelder, and H. Lüth, Journal of Appl. Phys 83 (8) 15 April 4324 (1998).

[7] E. A. de Andrada e Silva, G. C. La Rocca, and F. Bassani, Phys. Rev. B50, 8523 (1994).

[8] Y. Aharonov and D. Bohm, Phys. Rev. 115, 485 (1959).

[9] G. Bergmann, Phys. Rep. 107 (1) (1984); Phys. Rev. B 28, 2914 (1983).

[10] Thomas Heinzel, Mesoscopic Electronics in Solid State Nanostructures; Second edition. WILEY-VCH 2007, ISBN 978-527-40638-8.

[11] P.W. Anderson, Phys. Rev. 109, 1492 (1958).

[12] P. W. Anderson, E. Abrahams, and T. V. Ramakrishnan, Phys. Rev. Lett. 43, 718 (1979).

[13] M.Kohda, T.Bergsten and J.Nitta, Journal of the Physical Society of Japan **77**, No. 3, March, 031008, (2008).

[14] C. W. J. Beenakker and H. van Houten, Solid State Physics, 44, 1-228 (1991).

[15] G. Bergmann, Solid State Communications, Vol. 42, No. 11, pp. 815-817 (1982).

[16] L. E. Golub, Phy. Rev B 71, 235310 (2005).

[17] S. V. Iordanskii, Yu. B. Lyanda-Geller, and G. E. Pikus, Pis'ma, Zh. Eksp, Teor. Fiz. 60, 199 (1994); JETP Lett. 60, 206 (1994).

[18] Shinobu Hikami, Anatoly I. Larkin and Yosuke Nagaoka, Prog. Theor. Phys 63**,** No.2 (1980).

[19] F. G. Pikus and G. E. Pikus, Phys. Rev. B. 51, 16 928 (1995).

[20] M. A. Brand, A. Malinowski, O. Z. Karimov, P. A. Marsden, R.T. Harley, A. J.Shields, D. Sanvitto, D. A. Ritchie, and M. Y.Simmons, Phys. Rev. Lett. 89, 236601 (2002).

[21] J. B. Miller, D.M. Zumbühl, C.M. Marcus, Y. B. Lyanda-Geller, D. Goldhaber-Gordon,K. Campman, and A. C. Gossard, Phy. Rev. Lett 90, 7 (2003)..

[22] J M S Orr, P D Buckle, M Fearn, P J Wilding, C J Bartlett, MTEmeny, L Buckle and T Ashley, Semicond. Sci. Technol. 21**,** 1408–1411 (2006).

[23] T. Ashley, A. B. Dean, C. T. Elliott, G. J. Pryce, A. D. Johnson, and H. Willis, Appl. Phys. Lett. 66 (4), 23 January (1995).

[24] S. A. Solin, Tineke Thio, D. R. Hines, J. J. Heremans, *Science* 289, 1530 (2000).

[25] N. Goel, S. J. Chung, M. B. Santos, K. Suzuki, S. Miyashita and Y. Hirayama: Physica E (Amsterdam) 21, 761-764 (2004).

[26] Hong Chen, J.J. Hermans, J.A. Peters, A.O. Govorov, N. Goel, S.J. Chung and M.B. Santos, Appl. Phys. Lett. 86, 032113 (2005).

[27] http://www.ioffe.rssi.ru/SVA/NSM/Semicond/

[28] M. Edirisooriya, T. D. Mishima and M. B. Santos, J. Vac. Sci. Technol. B 25.3, 1063 (2007).

[29] T. D. Mishima and M. B. Santos, J. Vac. Sci. Technol. B 22.3 (2004).

[30] T. D. Mishima, J. C. Keay, N. Goel, M. A. Ball, S. J. Chung, M. B. Johnson, and M. B. Santos J. Vac. Sci. Technol. B 23.3 (2005).

[31] T. D. Mishima, M. Edirisooriya, and M. B. Santos, Apl Phys.Lett. 91, 062106 (2007).

[32] M. Cardona et al. Phys. Rev. B 38, 1806 (1988).

[33] http://groups.mrl.uiuc.edu/dvh/pdf/AZ5214E.pdf

[34] Rai-Choudhury: Handbook of Microlithography, Micromachining and Microfabrication, Volume PM39, ISBN-13: 978-0819423795.

[35] S. K. Ghandi, VLSI Fabrication Principles, Si and GaAs, Wiley, New York (1983)

[36] Zheng Cui, Nanofabrication: Principles, Capabilities and Limits, ISBN 0387755764, 9780387755762.

[37] R.J. Shul, S.J. Peartson: Handbook of advanced plasma processing techniques. ISBN 3-540-66772-5.

[38] J.R. Mileham, J.W. Lee, E.S. Lambers and S.J. Pearton, Semicond. Sci. Technol. 12 (1997) 338–344. Printed in the UK.

[39] S. A. Solin, D. R. Hines, J. S. Tsai, Yu. A. Pashkin, S. J. Chung, N. Goel, and M. B. Santos, IEEE Transactions on Magnetics, Vol. 38, NO. 1, January (2002).

[40] J. A. Diniz, J. W. Swart, K. B. Jung, J. Hong and S. J. Pearton, Solid-State Electronics Vol. 42, No. 11, 1947-1951 (1998).

[41] S. J. Pearton, U. K. Chakrabarti, F. Ren, C. R. Abernathy, A. Katz, W. S. Hobsonb and C. Constantine, Materials Science and Engineering, B25, 179-185 (1994).

[42] Mikael Karlsson, Fredrik Nikolajeff, Applied Optics, Vol. 41, No. 5 Feb (2002).

[43] Y. Z. Juang, Y. K. Su, S. J. Chang, D. F. Huang, and S. C. Chang, J. Vac. Sci. Technol. A 16.4, (1998).

[44] J. W. Lee, J. Hong, E. S. Lambers, C. R. Abernathy, S. J. Pearton, W. S. Hobson, and F. Ren, Plasma Chemistry and Plasma Processing, Vol. 17, No. 2. (1997).

[45] G. Allen Vawter and Joel R. Wendt, Appl. Phys. Lett. 58 (3), 21 January (1991).

[46] C. R. Paola, Solid-St. Electron. 13, 1189 (1970).

[47] T. Hassenkam, S. Pedersen, K. Baklanov, A. Kristensen, C. B. Sorensen, and P. E. Lindelof, F. G. Pikus, G. E. Pikus, Phys.Rev.B 55,15 (1997).

[48] W. Desrat and D. K. Maude, Z. R. Wasilewski, R. Airey and G. Hill, Phys. Rev B 74, 193317 (2006).

[49] Vitaliy A. Guzenko, Thomas Schäpers, and Hilde Hardtdegen, Phys. Rev B 76, 165301 (2007).

[50] S.A. Studenikin, P.T. Coleridge, P. Poole, Physica E 22, 349-352 (2004).

[51] C. Kurdak, N. Biyikli, Ü. Özgür, H. Morkoç, and V. I. Litvinov, Phy. Rev.B 74, 113308 (2006).

[52] N. Thillosen, S. Cabañas, N. Kaluza, V. A. Guzenko, H. Hardtdegen, and Th. Schäpers, Phys. Rev. B 73, 241311(R) (2006).

[53] B.L. Altshler, A.G Aronov, and D.E. Khmelnitsky, J. Phys. C15, 7367 (1982).

[54] H. Fukuyama and E. Abrahams, Phys. Rev. B 27, 5976 (1983).

[55] K. K. Choi_ and D. C. Tsui, Phys. Rev. B 36, 7751 - 7754 (1987).

[56] S. Pedersen, C. B. Sørensen, A. Kristensen, P. E. Lindelof, L. E. Golub and N. S. Averkiev, Phys. Rev. B 60, 7, 4880 (1999).

[57] Y. Avigal, J. Bregman,and Y. Shapira, J. Appl. Phys. 63, 430 (1988).

[58] Takaaki Koga, Junsaku Nitta, Tatsushi Akazaki, and Hideaki Takayanagi, Phy. Rev. Lett 89, 4 (2002).

[59] R. Winkler 'Spin-Orbit Coupling Effects in Two-Dimensional Electron and Hole Systems', Springer, (2003).

[60] H. van Houten, C. W. J. Beenakker, J. G. Williamson, M. E. I.Broekaart, P. H. M. van Loosdrecht, B. J. van Wees, J. E. Nooij,C. T. Foxon, and J. J. Harris, Phys. Rev. B 39, 8556 (1989).

[61] R. M. Potok, J. A. Folk, C. M. Marcus, and V. Umansky, Phys.Rev. Lett. 89, 266602 (2002).

[62] J. A. Folk, R. M. Potok, C. M. Marcus, and V. Umansky, Science 299, 679 (2003).

[63] J. R. Gao, 6. J. van Wees, J. J. Kuipers, J. P. Heida, and T. M. Klapwijk, Appl. Phys. Lett. 64 (19), 9 May (1994).

[64] R. H. Silsbee J. Phys.: Condens. Matter 16 R179–R207 (2004).

[65] L. P. Rokhinson, L. N. Pfeiffer, and K.W. West, Phys.Rev. Lett. 96, 156602 (2006).

[66] Jean Claude Chokomakoua Ph.D thesis, University of Oklahoma (2005).

[67] Semiconductor Spintronics and Quantum Computation, edited by D. Awschalom, N. Samarth, and D. Loss (Springer, New York 2002) ISBN13**:** 9783540421764.

[68] Peide D. Ye and Seigo Tarucha, Phys. Rev. B 59, 15-9794 (1999).

[69] Supriya Datta and Biswajit Das, Appl. Phys. Lett. 56, 7,665 (1990).

APPENDIX A

AZ5214 E Image reversal photolithography procedure

1. Clean the samples with acetone, methanol and isopropanol and blow dry with nitrogen.
2. Dehydration-bake at 150°C for 10 minutes.
3. Cool down the samples for 2 minutes on top an aluminum block.
4. Spin on AZ5214E resist at 4000 rpm for 40 seconds.
5. Pre-bake the samples at 95°C for 60 seconds.
6. Align and expose the pattern for 6.5 seconds (Karl-Suss MJB3 Mask Aligner).
7. Perform an image reversal-bake at 120°C for 90 seconds.
8. Cool down the samples for 2 minutes on top of an aluminum block.
9. Flood exposure for 60 seconds.
10. Develop pattern with MIF319 developer for 60 seconds.
11. De-ionized water rinse and blow dry.
12. After the desired fabrication process, the resist can be removed with an ultrasonic bath of 1165 remover (2-5 minutes).
13. De-ionized water rinse and blow dry.

APPENDIX B

UV113 e-beam lithography procedure

1. Clean the samples with acetone, methanol and isopropanol and blow dry with nitrogen.
2. Dehydration-bake at 150°C for 10 minutes.
3. Cool down the samples for 2 minutes on top of an aluminum block.
4. Spin on UV113 resist at 5000 rpm for 50 seconds.
5. Pre-bake the samples at 150°C for 60 seconds.
6. Pattern the samples with a 30KV e-beam at an optimum dose of 28 $\mu C/cm^2$ (For InSb dose optimization was performed on a RAITH 150 e-beam tool).
7. Post-exposure bake at 130°C for 90 seconds.
8. Develop patterns with DC 265 developer solution for 60 seconds.
9. De-ionized water rinse and blow dry.
10. After the desired fabrication process, the resist can be removed with an ultrasonic bath of 1165 remover (2-5 minutes).
11. De-ionized water rinse and blow dry.

APPENDIX C

Reactive ion etching recipes for InSb

- Optimized CH_4-H_2-Ar Recipe.
    - CH_4 flow rate = 3 sccm.
    - H_2 flow rate = 19 sccm.
    - Ar flow rate = 8 sccm.
    - Chamber pressure = 10 mTorr.
    - ICP power = 75 W.
    - RF power = 75 W.
    - Etch rate = 100 Å/min.

- Optimized BCl_3-Ar Recipe.
    - BCl_3 flow rate = 3 sccm
    - Ar flow rate = 12 sccm.
    - Chamber pressure = 3 mTorr.
    - ICP power = 50 W.
    - RF power = 100 W.
    - Etch rate = 700 Å/min.

APPENDIX D

Wire bonding parameters for Indium contacts on InSb

Parameter	Bond-1 (on PLCC)	Bond-2 (on In contact pad)
Search	1.44	1.44
Power	1.91	2.97
Time	4.9	3.4
Force	2.0	2.8

Parameter	Optimized setting
Tail	1.4
Tear	4.0
Step	0
Kink	0
Reverse	0
Y-speed	0
Loop	2.5